

# A Cosmological Signature of the SM Higgs Instability: Gravitational Waves

J. R. Espinosa,<sup>1,2,3</sup> D. Racco,<sup>4</sup> and A. Riotto<sup>4</sup>

<sup>1</sup>*Institut de Física d'Altes Energies (IFAE), The Barcelona Institute of Science and Technology (BIST),  
Campus UAB, 08193 Bellaterra, Barcelona, Spain*

<sup>2</sup>*ICREA, Institució Catalana de Recerca i Estudis Avançats,  
Passeig de Lluís Companys 23, 08010 Barcelona, Spain*

<sup>3</sup>*Instituto de Física Teórica IFT UAM/CSIC,  
Calle Nicolás Cabrera 13. UAM, Cantoblanco. 28049 Madrid, Spain*

<sup>4</sup>*Département de Physique Théorique and Centre for Astroparticle Physics (CAP),  
Université de Genève, 24 quai E. Ansermet, CH-1211 Geneva, Switzerland*

(Dated: Friday 24<sup>th</sup> May, 2019)

A fundamental property of the Standard Model is that the Higgs potential becomes unstable at large values of the Higgs field. For the current central values of the Higgs and top masses, the instability scale is about  $10^{11}$  GeV and therefore not accessible by colliders. We show that a possible signature of the Standard Model Higgs instability is the production of gravitational waves sourced by Higgs fluctuations generated during inflation. We fully characterise the two-point correlator of such gravitational waves by computing its amplitude, the frequency at peak, the spectral index, as well as their three-point correlators for various polarisations. We show that, depending on the Higgs and top masses, either LISA or the Einstein Telescope and Advanced-Ligo, could detect such stochastic background of gravitational waves. In this sense, collider and gravitational wave physics can provide fundamental and complementary informations. Since the mechanism described in this paper might also be responsible for the generation of dark matter under the form of primordial black holes, this latter hypothesis may find its confirmation through the detection of gravitational waves.

## Contents

<b>I. Introduction and description of the scenario</b>	<b>2</b>
<b>II. Equation of motion and its solution for Gravitational Waves</b>	<b>5</b>
Equation of motion of GWs	5
The source term for GWs	6
A compact expression for GWs with a numerical integration over time	7
<b>III. The power Spectrum of Gravitational Waves</b>	<b>8</b>
Two-point function of GWs	9
The energy density of GWs	10
<b>IV. Bispectrum of Gravitational Waves</b>	<b>11</b>
<b>V. Numerical results for the Energy Density and Bispectrum of GWs</b>	<b>12</b>
Energy density of GWs	12
The spectral tilt of GWs at low and high frequencies	14
The three-point correlator of GWs and its consistency relations	15
<b>VI. Conclusions</b>	<b>16</b>
<b>Appendices</b>	<b>18</b>
<b>Appendix A: Dynamics of the Higgs hitting the pole</b>	<b>18</b>
<b>Appendix B: Four and Six-Point Functions of the Curvature Perturbation</b>	<b>19</b>
Four-point function of the curvature perturbation	19
Six-point function of the curvature perturbation	20
<b>Appendix C: The final curvature perturbation in the radiation phase</b>	<b>20</b>

## I. INTRODUCTION AND DESCRIPTION OF THE SCENARIO

The recent detection of gravitational waves sourced by a spiralling binary system made of two  $\sim 30M_\odot$  black holes [1] has initiated the era of Gravitational Wave (GW) cosmology [2] and opened a new window to investigate the very early stages of the evolution of the Universe [3]. In particular, the Laser Interferometer Space Antenna (LISA) project [4], as well as the Einstein Telescope (ET) [5], Advanced-Ligo [6], and the Cosmic Explorer [7] at larger frequencies, will search for the stochastic gravitational wave background produced from different mechanisms, possibly identifying a primordial origin.

In this paper we point out that a stochastic background of gravitational waves may be the probe of one of the most fundamental properties of the Standard Model (SM) of weak interactions: the SM Higgs instability at high energies. Within the SM, the Higgs effective potential becomes deeper than the electroweak vacuum for large values of the Higgs background field when the quartic Higgs coupling  $\lambda$  becomes negative [8, 9]. For instance, this happens (by choosing the current central values of the Higgs and top masses) for Higgs field values of the order of  $\Lambda \simeq 10^{11}$  GeV. Despite this metastability condition of our present electroweak vacuum, its lifetime against decay both via quantum tunneling in flat spacetime or thermal fluctuations in the early Universe is by far longer than the age of the Universe [9, 10].

A natural and interesting question to ask is therefore which kind of physical phenomena might reveal, albeit indirectly, the presence of the SM instability. One option has been described in Ref. [11] and makes use of primordial inflation [12], the early stage during which the Universe expands exponentially and light fields may be quantum mechanically excited. The dynamics we consider can be conveniently divided in the following stages:

1. In the first phase the Higgs has an initial value much smaller than the instability scale  $\Lambda$ . However, if it is lighter than the Hubble rate  $H$ , the classical value of the Higgs  $h_c$  field keeps receiving each Hubble time kicks of the order of  $\pm(H/2\pi)$  and walks randomly. This dynamics is described by the stochastic equation [13]

$$\ddot{h}_c + 3H\dot{h}_c + V'(h_c) = 3H\eta, \quad V(h_c) \simeq -\frac{1}{4}\lambda h_c^4, \quad (1)$$

where  $\eta$  is a Gaussian random noise with

$$\langle \eta(t)\eta(t') \rangle = \frac{H^3}{4\pi^2} \delta(t-t'). \quad (2)$$

If the Hubble rate is large enough, the Higgs field can climb over the maximum of the potential and roll down to the unstable region [13–16].

2. In the second phase the Higgs has been pushed beyond the barrier of its effective potential and finds itself in the unbounded from below region. The motion starts being classically dominated over the quantum jumps at some time  $t_*$  if the classical displacement,  $(\Delta h)_{\text{cl}} \simeq V'/(3H^2)$  in a Hubble time, is larger than the quantum jumps  $(\Delta h)_{\text{q}} \simeq H/(2\pi)$ . This happens if the classical value of the Higgs  $h_c$  satisfies the relation

$$h_c^3 \gtrsim \frac{3H^3}{2\pi\lambda}. \quad (3)$$

During this stage the classical equation of motion reads

$$\ddot{h}_c + 3H\dot{h}_c + V'(h_c) = 0. \quad (4)$$

For convenience, we will focus on those patches where classicality takes over during the last stages of inflation, say the last 20  $e$ -folds or so. At the beginning of this phase, the motion of the Higgs is friction dominated,  $\ddot{h}_c \lesssim 3H\dot{h}_c$ . This happens as long as  $h_c^2 \lesssim 3H^2/\lambda$  and

$$h_c(t) \simeq \frac{h_*}{[1 - 2\lambda h_*^2(t - t_*)/3H]^1/2}, \quad (5)$$

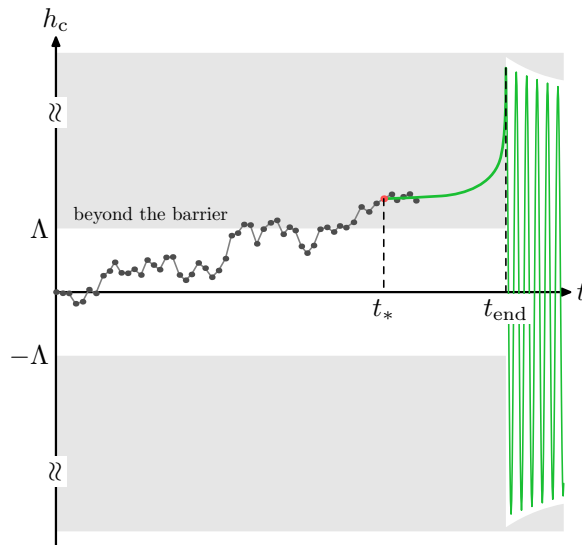


FIG. 1: Evolution of the Higgs field background  $h_c$  during inflation and reheating.

where  $t_*$  is the instant at which classicality takes over. When friction is subdominant,  $h_c$  rapidly increases

$$h_c(t) \simeq \frac{\sqrt{2}}{\sqrt{\lambda}} \frac{1}{(t_p - t)}, \quad (6)$$

where  $t_p$  is the time when the Higgs hits the pole (see Appendix A for more details).

3. The fast motion of the Higgs along the negative part of the potential may cause the patch of interest to experience an anti-de Sitter geometry which is potentially lethal. However, this situation can be rendered harmless and the patch end up to be our observed Universe if the reheating temperature  $T_{\text{RH}}$  after inflation is large enough to push the Higgs back to our current vacuum [11, 16, 17]. This happens because, thanks to the thermal interactions with the surrounding plasma, the Higgs potential is corrected to the form [16]

$$V_T \simeq \frac{1}{2} m_T^2 h_c^2, \quad m_T^2 \simeq 0.12 T^2 e^{-h_c/(2\pi T)}. \quad (7)$$

If the reheating temperature is large enough,  $T_{\text{RH}}^2 \gtrsim \lambda h_e^2$ , where  $h_e$  is the value of the Higgs when inflation ends, then the patch is rescued and the Higgs starts oscillating (with a relativistic equation of state) around the current electroweak vacuum where it will settle after a while.

Fig. 1 summarises the dynamics of the classical value of the Higgs during the various stages. Meanwhile, the perturbations of the Higgs field are excited and during inflation they satisfy the following equation of motion (in the flat gauge)

$$\delta \ddot{h}_k + 3H \delta \dot{h}_k + \frac{k^2}{a^2} \delta h_k + V''(h_c) \delta h_k = \frac{\delta h_k}{a^3 m_{\text{P}}^2} \frac{d}{dt} \left( \frac{a^3}{H} \dot{h}_c^2 \right), \quad (8)$$

where  $a$  is the scale factor,  $m_{\text{P}}$  is the reduced Planck mass, and the last term accounts for the backreaction of the metric perturbations. These perturbations are born inside the Hubble radius with the standard Bunch-Davies vacuum,  $\delta h_k(k \gg aH) = (1/a\sqrt{2k})e^{-ik/aH}$  and, as soon as their physical wavelength becomes larger than the Hubble radius, they rapidly grow driven by the rolling down of the Higgs field [11]

$$\delta h_k(k \ll aH) = \frac{H}{\sqrt{2k^3}} \frac{\dot{h}_c(t)}{\dot{h}_c(t_k)}. \quad (9)$$

For the wavelengths leaving the Hubble radius the last 20  $e$ -folds or so of inflation, the gauge-invariant comoving curvature perturbation  $\zeta(\vec{x})$  is dominated by the Higgs perturbations and reads

$$\zeta \simeq \frac{\dot{\rho}_h}{\dot{\rho}} \zeta_h, \quad \zeta_h \simeq H \frac{\delta \rho_h}{\dot{\rho}_h}, \quad (10)$$

(still in the flat gauge and we do not write down the subdominant standard component that is responsible for the cosmic microwave background anisotropies on much larger scales). Since the Higgs energy-momentum tensor is separately (covariantly) conserved during inflation,  $\zeta_h$  is conserved on super-Hubble scales and freezes in at the value [11]

$$\dot{\zeta}_h(k \ll aH) = 0 \text{ and } \zeta_h(k \ll aH) = \frac{H^2}{\sqrt{2k^3 \dot{h}_c(t_k)}}, \quad k = a(t_k)H. \quad (11)$$

After inflation ends, there is a fast transient epoch of reheating during which the long wavelength Higgs perturbations are subject to energy transfer involving the thermal plasma as their effective mass suddenly jumps to its thermal value induced by the interactions with the plasma. After reheating is over the Higgs perturbations promptly decay into radiation curvature perturbations which subsequently remain constant on super-Hubble scales as well (see Appendix C for a more detailed discussion). Upon Hubble reentry, if sizeable enough, these perturbations source high peaks in the matter power spectrum which collapse to form Primordial Black Holes (PBHs). A first cosmological signature of the electroweak instability could be therefore that the dark matter (or a fraction thereof) is under the form of PBHs seeded by Higgs fluctuations during inflation [11]. In this scenario, no physics beyond the Standard Model should be invoked to explain the dark matter in our observed Universe, but anthropic arguments are necessary to explain the fine-tuning on the initial conditions.

In this paper we propose that a second signature of the SM instability might be a stochastic background of gravitational waves potentially detectable by the space-based interferometer LISA. Indeed, if there are large Higgs perturbations generated during the last stages of inflation, responsible or not for the PBHs as dark matter, they inevitably act as a (second-order) source of primordial gravitational waves at horizon reentry. The goal of this paper is therefore to

1. characterize the two-point correlator (power spectrum  $\mathcal{P}_h$ , its tilt as well as the frequency at the peak) of gravitational waves induced by the first-order Higgs perturbations. Parametrically one expects  $\mathcal{P}_h \sim \mathcal{P}_\zeta^2$  at Hubble crossing and therefore one can reach values of  $\mathcal{P}_h$  as large as  $10^{-4}$ ; the spectral tilt is also particularly interesting as the GW spectrum usually covers a large range of frequencies. The study of the detectability of the spectral index of a generic GW background with energy density  $\Omega_{\text{GW}}(f) = A(f/f_*)^{n_T}$  can be found in Ref. [4] as a function of the frequency at the peak. For a signal peaked at  $f_* \sim 0.05$  Hz and  $A \sim 10^{-12}$  one could constrain  $n_T \lesssim \mathcal{O}(1)$  and  $n_T \gtrsim \mathcal{O}(7)^1$ ;
2. calculate the three-point correlator (bispectrum  $B_h$ ) of the gravitational waves induced by the first-order Higgs perturbations. Parametrically one expects  $B_h \sim \mathcal{P}_\zeta^3$  at Hubble crossing. Such a non-Gaussian signal, despite its presence in the primordial bispectrum, is unfortunately not observable today in a detector which collects signal simultaneously from all patches of the sky, as discussed in [18].

We will see that

1. the energy density  $\Omega_{\text{GW}}$  of the GWs generated by the Higgs fluctuations is typically of the order of  $10^{-8}$  at the peak. The latter is reached at frequencies ranging from  $10^{-2}$  to 10 Hz. This should allow either LISA or ET and Advanced-Ligo to detect the signal. Furthermore, as the frequency at the peak depends sensitively on the Higgs and top mass, this will provide complementary and fundamental information to be crossed with the ones provided by colliders with the possibility of either confirming or ruling out the origin of the GW signal;
2. the spectral index of the signal will have a characteristic behaviour: blue with  $n_T \simeq 3$  for frequencies below the peak, and red with  $n_T \simeq -0.6$  for frequencies above the peak frequency;
3. the bispectrum, in the case in which the two-point correlator is detectable by LISA, is mainly peaked in the so-called equilateral configurations. Summing up all polarisations we find the characteristic consistency relation  $(k_1 k_2 k_3)^2 B_h \sim 3 \cdot 10^4 \mathcal{P}_h^{3/2}$ . This non-Gaussian part of the GW signal is unfortunately unobservable in a GW detector, which unavoidably measures the sum of the signal from many uncorrelated patches of the sky. This sum is Gaussian by means of the Central Limit Theorem, and no bispectrum can be observed for any primordial GW background [18].

---

<sup>1</sup> For a frequency at the peak of  $f_{\text{CMB}} \sim 7.7 \cdot 10^{-17}$  Hz, present CMB data already provide an upper bound on the amount of GWs,  $\Omega_{\text{GW}}^{\text{CMB}}$ , generated during inflation and one can write the GW energy density  $\Omega_{\text{GW}} = \Omega_{\text{GW}}^{\text{CMB}} (f/f_{\text{CMB}})^{n_T}$ , being  $n_T$  the spectral tilt. A limit of  $n_T \lesssim 0.35$  can be obtained for the best LISA configuration with six links, five million km arm length and a five year mission [4].

The paper is organised as follows. In section II we describe the equation of motion for the GWs and its solution; in section III we compute the power spectrum of the GWs, while their bispectrum is calculated in section IV. Numerical results are found in section V and in section VI we conclude. The paper contains also various Appendices with extra useful material.

## II. EQUATION OF MOTION AND ITS SOLUTION FOR GRAVITATIONAL WAVES

Our goal is to evaluate the amount of gravitational waves produced during the radiation phase by the SM Higgs perturbations which in turn owe their origin to the previous period of inflation. The correct formalism to evaluate the contribution to the generation at second-order of tensor modes from first-order scalar perturbations has been first discussed in [19–22]. The first two parts of this section follow quite closely the notation of Appendix A of [24]. Our convention for the signature of the metric is  $(-+++)$ , so that the perturbed metric in the conformal Newtonian gauge reads

$$ds^2 = -a^2(1 + 2\Phi)d\eta^2 + a^2 \left[ (1 - 2\Psi)\delta_{ij} + \frac{1}{2}h_{ij} \right] dx^i dx^j, \quad (12)$$

where  $\Phi$ ,  $\Psi$  are the Bardeen potentials and the tensor perturbations  $h_{ij}$  are transverse and traceless:  $\partial_i h_{ij} = h_{ii} = 0$ . In absence of anisotropy in the stress-energy tensor, we have  $\Phi = \Psi$  (including stress gives only a small correction [22]). Furthermore, one can rewrite  $h_{ij}$  in terms of the basis  $\{e_{ij}^{(+)}, e_{ij}^{(\times)}\}$  of polarisation tensors as follows

$$h_{ij}(\eta, \mathbf{x}) = \int \frac{d^3k}{(2\pi)^3} \left[ h_{\mathbf{k}}^{(+)}(\eta) e_{ij}^{(+)}(\mathbf{k}) + h_{\mathbf{k}}^{(\times)}(\eta) e_{ij}^{(\times)}(\mathbf{k}) \right] e^{i\mathbf{k}\cdot\mathbf{x}}. \quad (13)$$

The polarisation basis is given by

$$e_{ij}^{(+)}(\mathbf{k}) = \frac{1}{\sqrt{2}} [e_i(\mathbf{k})e_j(\mathbf{k}) - \bar{e}_i(\mathbf{k})\bar{e}_j(\mathbf{k})], \quad (14)$$

$$e_{ij}^{(\times)}(\mathbf{k}) = \frac{1}{\sqrt{2}} [e_i(\mathbf{k})\bar{e}_j(\mathbf{k}) + \bar{e}_i(\mathbf{k})e_j(\mathbf{k})], \quad (15)$$

where  $e_i(\mathbf{k})$  and  $\bar{e}_i(\mathbf{k})$  are two three-dimensional vectors orthonormal to  $\mathbf{k}$ , and the normalisation factor guarantees that  $e_{ij}^{(+)}e_{ij}^{(+)} = e_{ij}^{(\times)}e_{ij}^{(\times)} = 1$ ,  $e_{ij}^{(+)}e_{ij}^{(\times)} = 0$ .

### Equation of motion of GWs

The equation of motion for the GWs is obtained by extracting the tensor component of the Einstein equations expanded up to second order in perturbations

$$h_{ij}'' + 2\mathcal{H}h_{ij}' - \nabla^2 h_{ij} = -4\mathcal{T}_{ij}{}^{lm} \mathcal{S}_{lm}, \quad (16)$$

where  $'$  denotes the derivative with respect to conformal time,  $\mathcal{H} = a'/a$  is the conformal Hubble parameter,  $\mathcal{S}_{lm}$  is the source term defined below in Eq. (22). The projector  $\mathcal{T}_{ij}{}^{lm}$  acting on the source term selects its transverse and traceless part. We define it in Fourier space (and use  $\hat{\phantom{x}}$ , when needed, to denote quantities in the conjugate space) as

$$\hat{\mathcal{T}}_{ij}{}^{lm}(\mathbf{k}) = e_{ij}^{(+)}(\mathbf{k}) e^{(+)lm}(\mathbf{k}) + e_{ij}^{(\times)}(\mathbf{k}) e^{(\times)lm}(\mathbf{k}). \quad (17)$$

Our convention for the Fourier transform is the following:

$$\mathcal{S}_{lm}(\eta, \mathbf{x}) = \int \frac{d^3k}{(2\pi)^3} \hat{\mathcal{S}}_{lm}(\eta, \mathbf{k}) e^{i\mathbf{k}\cdot\mathbf{x}}, \quad (18)$$

so that the equation of motion (16) reads, for each polarisation mode  $s = (+), (\times)$ ,

$$h_{\mathbf{k}}^s{}''(\eta) + 2\mathcal{H} h_{\mathbf{k}}^s{}'(\eta) + k^2 h_{\mathbf{k}}^s(\eta) = \hat{\mathcal{S}}^s(\eta, \mathbf{k}), \quad (19)$$

where  $\widehat{\mathcal{S}}^s(\eta, \mathbf{k}) \equiv -4 e^{s,lm}(\mathbf{k}) \widehat{\mathcal{S}}_{lm}(\eta, \mathbf{k})$ . The method of the Green function yields the solution

$$h_{\mathbf{k}}^s(\eta) = \frac{1}{a(\eta)} \int^{\eta} d\tilde{\eta} g_{\mathbf{k}}(\eta, \tilde{\eta}) a(\tilde{\eta}) \widehat{\mathcal{S}}^s(\tilde{\eta}, \mathbf{k}), \quad (20)$$

where the Green function  $g_{\mathbf{k}}(\eta, \tilde{\eta})$  for a radiation-dominated (RD) Universe is

$$g_{\mathbf{k}}(\eta, \tilde{\eta}) = \frac{\sin[k(\eta - \tilde{\eta})]}{k} \theta(\eta - \tilde{\eta}), \quad (21)$$

$\theta$  being the Heaviside step function.

### The source term for GWs

The source term  $\widehat{\mathcal{S}}_{ij}$  for GWs appearing in Eq. (16) arises at second order in the scalar perturbation  $\Psi$  [19]

$$\mathcal{S}_{ij} = 4\Psi\partial_i\partial_j\Psi + 2\partial_i\Psi\partial_j\Psi - \frac{4}{3(1+w)}\partial_i\left(\frac{\Psi'}{\mathcal{H}} + \Psi\right)\partial_j\left(\frac{\Psi'}{\mathcal{H}} + \Psi\right), \quad (22)$$

where  $w$  is the equation of state of the fluid permeating the Universe at a given epoch. Since the generation of GWs occurs mainly when the relevant modes re-enter the Hubble radius, which for the modes of our interest happens deeply into the RD era, we specialise to  $w = 1/3$ . We rewrite the source in Fourier space, introducing

$$\widehat{\Psi}(\eta, \mathbf{k}) = \int d^3x \Psi(\eta, \mathbf{x}) e^{-i\mathbf{k}\cdot\mathbf{x}} \quad (23)$$

so the right hand side of Eq. (19) becomes (we omit the temporal dependence for brevity)

$$\widehat{\mathcal{S}}^s(\eta, \mathbf{k}) = 4 \int \frac{d^3p}{(2\pi)^3} e^{s,ij}(\mathbf{k}) p_i p_j \left[ 2\widehat{\Psi}(\mathbf{p})\widehat{\Psi}(\mathbf{k}-\mathbf{p}) + \left(\widehat{\Psi}(\mathbf{p}) + \frac{1}{\mathcal{H}}\widehat{\Psi}'(\mathbf{p})\right) \left(\widehat{\Psi}(\mathbf{k}-\mathbf{p}) + \frac{1}{\mathcal{H}}\widehat{\Psi}'(\mathbf{k}-\mathbf{p})\right) \right]. \quad (24)$$

The expression inside squared brackets is explicitly symmetric under the exchange of  $\mathbf{p}$  and  $\mathbf{k}-\mathbf{p}$ .

The scalar perturbation  $\Psi(\eta, \mathbf{k})$  is directly related to the gauge invariant comoving curvature perturbation by  $\Psi = \frac{2}{3}\zeta$  [12]. We define then the transfer function  $T(\eta, k)$  through the relation

$$\widehat{\Psi}(\eta, \mathbf{k}) = \frac{2}{3}T(\eta, k)\zeta(\mathbf{k}), \quad (25)$$

and its expression is given in the RD era by

$$T(\eta, k) = \mathcal{T}(k\eta), \quad \mathcal{T}(z) = \frac{9}{z^2} \left[ \frac{\sin(z/\sqrt{3})}{z/\sqrt{3}} - \cos(z/\sqrt{3}) \right]. \quad (26)$$

We can rewrite the source term (24) as

$$\widehat{\mathcal{S}}^s(\eta, \mathbf{k}) = \frac{4}{9} \int \frac{d^3p}{(2\pi)^3} e^s(\mathbf{k}, \mathbf{p}) f(p, |\mathbf{k}-\mathbf{p}|, \eta) \zeta(\mathbf{p})\zeta(\mathbf{k}-\mathbf{p}), \quad (27)$$

where we have introduced

$$e^s(\mathbf{k}, \mathbf{p}) \equiv e^{s,ij}(\mathbf{k}) p_i p_j = \begin{cases} \frac{1}{\sqrt{2}} p^2 \sin^2 \theta \cos 2\phi & \text{for } s = (+), \\ \frac{1}{\sqrt{2}} p^2 \sin^2 \theta \sin 2\phi & \text{for } s = (\times), \end{cases} \quad (28)$$

where  $(p, \theta, \phi)$  are the coordinates of  $\mathbf{p}$  in a spherical coordinate system whose  $(\hat{x}, \hat{y}, \hat{z})$  axes are aligned with  $(e(\mathbf{k}), \bar{e}(\mathbf{k}), \mathbf{k})$ , and

$$f(k_1, k_2, \eta) \equiv 4 \left[ 2T(\eta, k_1)T(\eta, k_2) + \left(T(\eta, k_1) + \frac{1}{\mathcal{H}}T'(\eta, k_1)\right) \left(T(\eta, k_2) + \frac{1}{\mathcal{H}}T'(\eta, k_2)\right) \right]. \quad (29)$$

### A compact expression for GWs with a numerical integration over time

Let us rewrite the solution for the GWs  $h_{\mathbf{k}}^s(\eta)$  by collecting the results of (20), (21), (27)

$$\begin{aligned} h_{\mathbf{k}}^s(\eta) &= \frac{1}{a(\eta)} \int^{\eta} d\tilde{\eta} \frac{\sin(k\eta) \cos(k\tilde{\eta}) - \cos(k\eta) \sin(k\tilde{\eta})}{k} a(\tilde{\eta}) \frac{4}{9} \int \frac{d^3p}{(2\pi)^3} e^s(\mathbf{k}, \mathbf{p}) f(p, |\mathbf{k} - \mathbf{p}|, \tilde{\eta}) \zeta(\mathbf{p}) \zeta(\mathbf{k} - \mathbf{p}) = \\ &= \frac{4}{9} \int \frac{d^3p}{(2\pi)^3} \frac{1}{k^3 \eta} e^s(\mathbf{k}, \mathbf{p}) \zeta(\mathbf{p}) \zeta(\mathbf{k} - \mathbf{p}) \left[ \int^{\eta} k d\tilde{\eta} (k\tilde{\eta}) \left( \sin(k\eta) \cos(k\tilde{\eta}) - \cos(k\eta) \sin(k\tilde{\eta}) \right) f(p, |\mathbf{k} - \mathbf{p}|, \tilde{\eta}) \right], \end{aligned} \quad (30)$$

where we have expressed the scale factor in terms of conformal time during RD,  $a(\tilde{\eta})/a(\eta) = \tilde{\eta}/\eta$ .

The tensor modes begin to be generated at the time at which the wavelength  $1/k$  re-enters the comoving Hubble radius, given that the source is damped on super-Hubble scales. We provide in Appendix D the analytical results both for a generic lower extreme of integration  $\eta_{\text{in}}$  and for two values which are equivalent in practice:  $\eta_{\text{in}} = 0$  (strictly speaking, the exact result) and  $\eta_{\text{in}} = k^{-1}$ , which is the value that is chosen for the numerical results in the remainder of the paper. The transfer function (26) decays as  $\eta^{-2}$ , so that the generation of tensor modes is completed within a time which is a few orders of magnitude larger than  $k^{-1}$ , around  $\eta \sim \mathcal{O}(10^3)k^{-1}$ . Therefore the extrema of the integral over  $\tilde{\eta}$  in Eq. (30) are  $\tilde{\eta} = \eta_{\text{in}}$  and the current time  $\eta \gg \mathcal{O}(10^3)k^{-1}$ , so that we can approximate it to  $\tilde{\eta} \rightarrow \infty$ .

The dimensionless expression contained in square brackets in Eq. (30) can be computed analytically, in order to facilitate the calculation of the two- and three-point functions. We denote

$$x = \frac{p}{k}, \quad y = \frac{|\mathbf{k} - \mathbf{p}|}{k}, \quad (31)$$

and we use the dimensionless time variable  $\tau \equiv k\tilde{\eta}$ , and we input the Hubble rate  $\mathcal{H} = aH = \eta^{-1}$  during RD. We can then rewrite Eq. (30) as

$$h_{\mathbf{k}}^s(\eta) = \frac{4}{9} \int \frac{d^3p}{(2\pi)^3} \frac{1}{k^3 \eta} e^s(\mathbf{k}, \mathbf{p}) \zeta(\mathbf{p}) \zeta(\mathbf{k} - \mathbf{p}) \left[ \mathcal{I}_c(x, y) \cos(k\eta) + \mathcal{I}_s(x, y) \sin(k\eta) \right], \quad (32)$$

where we have introduced two functions,  $\mathcal{I}_c$  and  $\mathcal{I}_s$ , that can be computed analytically (the reader can find the analytical result in Appendix D)

$$\begin{aligned} \mathcal{I}_c(x, y) &= \int_{\eta_{\text{in}}}^{\infty} d\tau \tau (-\sin \tau) \cdot 4 \left\{ 2\mathcal{T}(x\tau)\mathcal{T}(y\tau) + \left[ \mathcal{T}(x\tau) + x\tau \mathcal{T}'(x\tau) \right] \left[ \mathcal{T}(y\tau) + y\tau \mathcal{T}'(y\tau) \right] \right\}, \\ \mathcal{I}_s(x, y) &= \int_{\eta_{\text{in}}}^{\infty} d\tau \tau (\cos \tau) \cdot 4 \left\{ 2\mathcal{T}(x\tau)\mathcal{T}(y\tau) + \left[ \mathcal{T}(x\tau) + x\tau \mathcal{T}'(x\tau) \right] \left[ \mathcal{T}(y\tau) + y\tau \mathcal{T}'(y\tau) \right] \right\}. \end{aligned} \quad (33)$$

The domain in the  $(x, y)$  plane is shown in the left plot of Fig. 2: it consists of the configurations allowed by the triangular inequality applied to the triangle formed by the vectors  $\mathbf{k}$ ,  $\mathbf{p}$ ,  $\mathbf{k} - \mathbf{p}$ , and is given by

$$(x + y \geq 1) \wedge (x + 1 \geq y) \wedge (y + 1 \geq x). \quad (34)$$

It is useful to introduce two auxiliary variables  $(d, s)$  in terms of  $(x, y)$ , which simplify the expression of  $\mathcal{I}_c, \mathcal{I}_s$  for the purpose of an analytical integration,

$$d = \frac{1}{\sqrt{3}}|x - y|, \quad s = \frac{1}{\sqrt{3}}(x + y), \quad (d, s) \in [0, 1/\sqrt{3}] \times [1/\sqrt{3}, +\infty) \quad (35)$$

This redefinition of domain is illustrated in Fig. 2.

The result for the analytical calculation of the integrals  $\mathcal{I}_c, \mathcal{I}_s$  for each point  $(d, s)$  is shown in Figs. 3 and 4.

We observe that the numerical value of  $\mathcal{I}_c(d, s), \mathcal{I}_s(d, s)$  is nearly independent of  $d = |x - y|/\sqrt{3}$ . More interestingly, the integrals  $\mathcal{I}_c, \mathcal{I}_s$  are spiked for a value of  $s \sim 1$  corresponding to  $p + |\mathbf{k} - \mathbf{p}| \sim \sqrt{3}k$ . The reason for this is that the integrands of  $\mathcal{I}_c$  and  $\mathcal{I}_s$  are products of trigonometric functions of  $\tau$  times a rational function of  $\tau$ , and the oscillating behaviour determines cancellations in the final result. Only for  $p + |\mathbf{k} - \mathbf{p}| \sim \sqrt{3}k$  there appear some terms in the integrand with the square of a trigonometric function and thus with a definite sign, and this increases the final result. Notice that the factor  $\sqrt{3}$  is simply due to the factor  $\sqrt{w}$  appearing in the arguments of the transfer function of Eq. (26), and not to geometrical reasons.

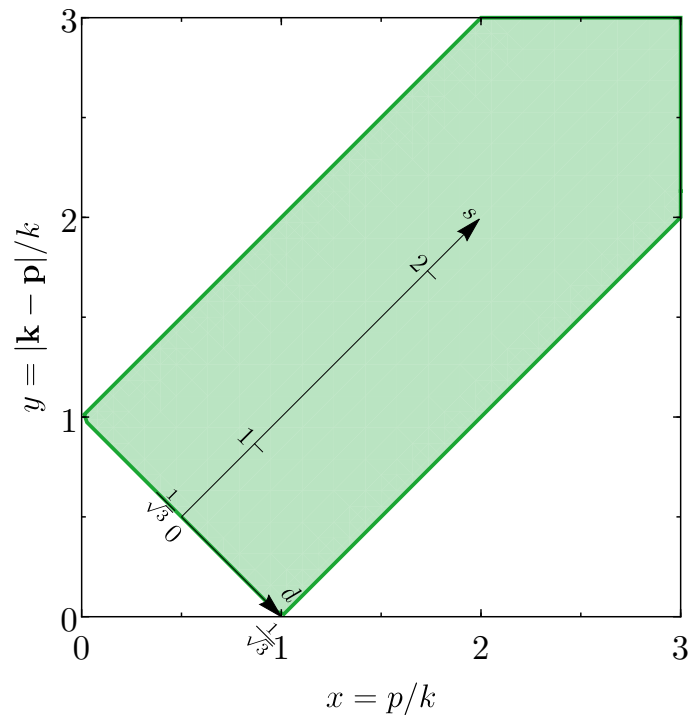


**FIG. 2:** Domain for the variables  $x = p/k$ ,  $y = |\mathbf{k} - \mathbf{p}|/k$  allowed by the triangular inequality, superimposed with the  $(d, s)$  coordinates defined in Eq. (35).

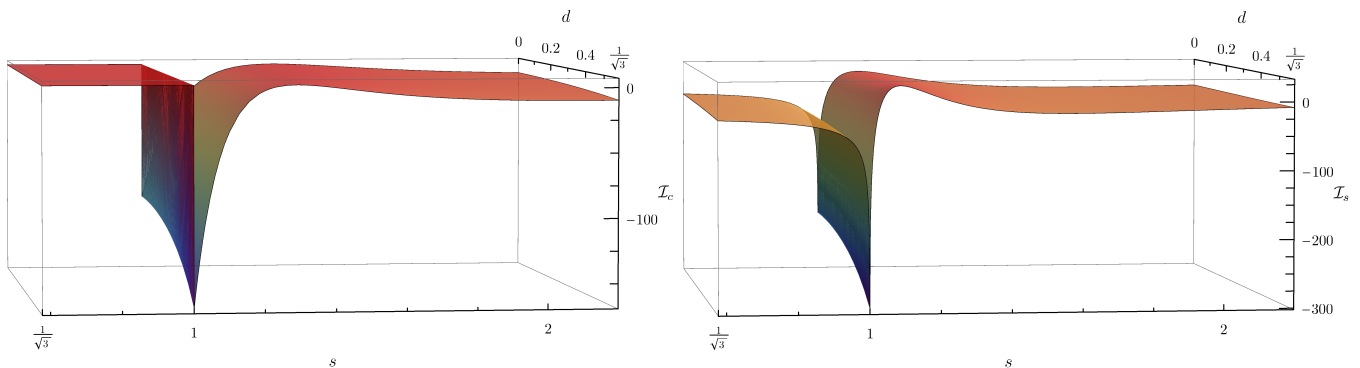


**FIG. 3:** 3D plots of  $\mathcal{I}_c$  (left plot) and  $\mathcal{I}_s$  (right plot), defined in Eq. (33), as a function of  $(d, s)$  (Eq. (35)).

### III. THE POWER SPECTRUM OF GRAVITATIONAL WAVES

In this section we present the generic derivation of the two-point function and the power spectrum of gravitational waves. This result has been already derived and exposed in Refs. [19–22]. The goal of the present section is to match it with our notation, and to prepare an analogous derivation of the three-point function of GWs in the next section. In section V we will use the formulæ obtained here to calculate the power spectrum and the three-point function of GWs generated in our scenario.



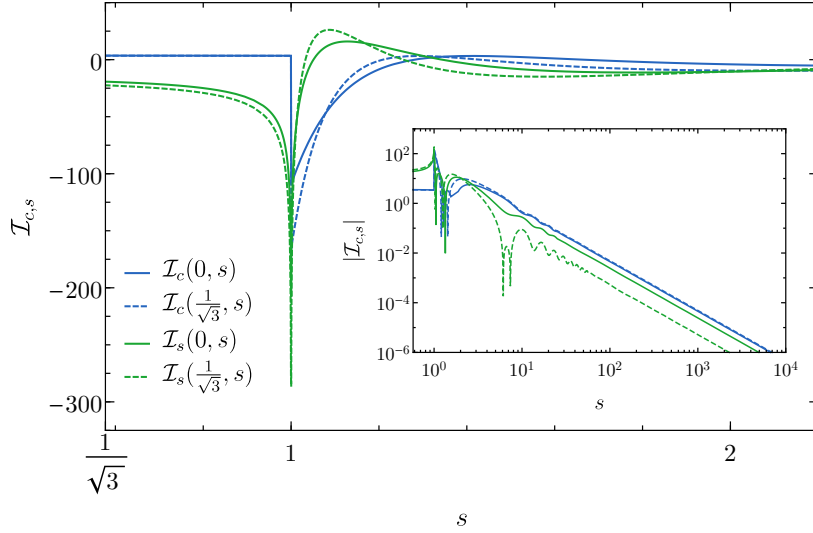


**FIG. 4:** Behaviour of the integrals  $\mathcal{I}_c$ ,  $\mathcal{I}_s$ , defined in Eq. (33), as a function of  $s$  (Eq. (35)), for the two extremal values of  $d = |x - y|/\sqrt{3}$ .

### Two-point function of GWs

We begin by writing the definition of two-point function, with the use of Eq. (32)

$$\langle h^r(\eta, \mathbf{k}_1) h^s(\eta, \mathbf{k}_2) \rangle = \left(\frac{4}{9}\right)^2 \int \frac{d^3 p_1}{(2\pi)^3} \int \frac{d^3 p_2}{(2\pi)^3} \frac{1}{k_1^3 k_2^3 \eta^2} e^r(\mathbf{k}_1, \mathbf{p}_1) e^s(\mathbf{k}_2, \mathbf{p}_2) \langle \zeta(\mathbf{p}_1) \zeta(\mathbf{k}_1 - \mathbf{p}_1) \zeta(\mathbf{p}_2) \zeta(\mathbf{k}_2 - \mathbf{p}_2) \rangle \cdot [\cos(k_1 \eta) \mathcal{I}_c(x_1, y_1) + \sin(k_1 \eta) \mathcal{I}_s(x_1, y_1)] [\cos(k_2 \eta) \mathcal{I}_c(x_2, y_2) + \sin(k_2 \eta) \mathcal{I}_s(x_2, y_2)], \quad (36)$$

where  $x_i = p_i/k_i$ ,  $y_i = |\mathbf{k}_i - \mathbf{p}_i|/k_i$ . To evaluate the four-point function of the curvature perturbation  $\zeta$  we proceed as usual, noting that at leading order it is a Gaussian variable defined by the dimensionless power spectrum  $\mathcal{P}_\zeta$

$$\langle \zeta(\mathbf{k}_1) \zeta(\mathbf{k}_2) \rangle \equiv (2\pi)^3 \delta^{(3)}(\mathbf{k}_1 + \mathbf{k}_2) \frac{2\pi^2}{k_1^3} \mathcal{P}_\zeta(k_1), \quad (37)$$

and the four-point function of  $\zeta$  of the first line of (36) has two possible non-vanishing contractions for  $\mathbf{k}_1, \mathbf{k}_2 \neq 0$ . The two contributions give the same result, given that they correspond to each other up to a shift  $\mathbf{p}_2 \rightarrow (\mathbf{k}_2 - \mathbf{p}_2)$ , which is a symmetry of Eq. (36), see Appendix B for details. We can evaluate then Eq. (36) for any of the two configurations, and multiply the final result by 2. After integrating over  $\mathbf{p}_2$  one gets

$$\langle h^r(\eta, \mathbf{k}_1) h^s(\eta, \mathbf{k}_2) \rangle = (2\pi)^3 \delta^{(3)}(\mathbf{k}_1 + \mathbf{k}_2) \cdot 2 \left(\frac{4}{9}\right)^2 \int \frac{d^3 p_1}{(2\pi)^3} \frac{1}{k_1^6 \eta^2} e^r(\mathbf{k}_1, \mathbf{p}_1) e^s(\mathbf{k}_1, \mathbf{p}_1) \frac{2\pi^2}{p_1^3} \frac{2\pi^2}{|\mathbf{k}_1 - \mathbf{p}_1|^3} \cdot \mathcal{P}_\zeta(p_1) \mathcal{P}_\zeta(|\mathbf{k}_1 - \mathbf{p}_1|) [\cos^2(k_1 \eta) \mathcal{I}_c(x_1, y_1)^2 + \sin^2(k_1 \eta) \mathcal{I}_s(x_1, y_1)^2 + \sin(2k_1 \eta) \mathcal{I}_c(x_1, y_1) \mathcal{I}_s(x_1, y_1)]. \quad (38)$$

Let us refer to a system of spherical coordinates  $(p_1, \theta, \phi)$  oriented around the axis  $\mathbf{k}_1$ , and denote  $x \equiv x_1 = p_1/k_1$ ,  $y \equiv y_1 = |\mathbf{k}_1 - \mathbf{p}_1|/k_1$ . In these variables one has  $\mathbf{p}_1 = (k_1 x, \cos^{-1}((1+x^2-y^2)/2x), \phi)$ . We perform the following change of integration variables

$$\int d^3 p_1 \longrightarrow k_1^3 \iint_{\mathcal{S}} dx dy x^2 \frac{y}{x} \int_0^{2\pi} d\phi, \quad (39)$$

where  $\mathcal{S}$  is the infinite strip shown in Fig. 2. The integral over  $\phi$  can be easily solved analytically, and selects only some of the possible couples of polarisations  $(r, s)$  to give a non-vanishing result. With the use of Eq. (28) we obtain

$$\int_0^{2\pi} d\phi e^r(\mathbf{k}_1, \mathbf{p}_1) e^s(\mathbf{k}_1, \mathbf{p}_1) = \frac{k_1^4}{2} x^4 \left[ 1 - \frac{(1+x^2-y^2)^2}{4x^2} \right]^2 \cdot \pi \delta^{rs}. \quad (40)$$

By collecting the results of the last three equations we get the final expression for the two-point function of GWs:

$$\begin{aligned} \langle h^r(\eta, \mathbf{k}_1) h^s(\eta, \mathbf{k}_2) \rangle &= (2\pi)^3 \delta^{(3)}(\mathbf{k}_1 + \mathbf{k}_2) \frac{2\pi^2}{k_1^3} \delta^{rs} \cdot 2 \left( \frac{4}{9} \right)^2 \frac{1}{k_1^2 \eta^2} \iint_{\mathcal{S}} dx dy \frac{x^2}{8y^2} \left[ 1 - \frac{(1+x^2-y^2)^2}{4x^2} \right]^2 \\ &\cdot \mathcal{P}_\zeta(k_1 x) \mathcal{P}_\zeta(k_1 y) \left[ \cos^2(k_1 \eta) \mathcal{I}_c(x, y)^2 + \sin^2(k_1 \eta) \mathcal{I}_s(x, y)^2 + \sin(2k_1 \eta) \mathcal{I}_c(x, y) \mathcal{I}_s(x, y) \right]. \end{aligned} \quad (41)$$

The integrand is explicitly symmetric under exchange of  $x$  and  $y$ . From Eq. (41) and the definition of the power spectrum of GWs

$$\langle h^r(\eta, \mathbf{k}_1) h^s(\eta, \mathbf{k}_2) \rangle \equiv (2\pi)^3 \delta^{(3)}(\mathbf{k}_1 + \mathbf{k}_2) \delta^{rs} \frac{2\pi^2}{k_1^3} \mathcal{P}_h(k_1) \quad (42)$$

we can extract  $\mathcal{P}_h(\eta, k)$ :

$$\mathcal{P}_h(\eta, k) = \frac{4}{81} \frac{1}{k^2 \eta^2} \iint_{\mathcal{S}} dx dy \frac{x^2}{y^2} \left[ 1 - \frac{(1+x^2-y^2)^2}{4x^2} \right]^2 \mathcal{P}_\zeta(kx) \mathcal{P}_\zeta(ky) \left[ \cos^2(k\eta) \mathcal{I}_c^2 + \sin^2(k\eta) \mathcal{I}_s^2 + \sin(2k\eta) \mathcal{I}_c \mathcal{I}_s \right], \quad (43)$$

where for brevity we do not write the arguments of the functions  $\mathcal{I}_c(x, y)$  and  $\mathcal{I}_s(x, y)$ , defined in Eq. (33) and plotted in Figs. 3 and 4.

### The energy density of GWs

In this section we derive the expression for the energy density of GWs, and its fraction  $\Omega_{\text{GW}}$  relative to the critical energy density. The energy density of GWs is [25]

$$\rho_{\text{GW}}(\eta, \mathbf{x}) = \frac{m_P^2}{16a^2(\eta)} \left\langle \frac{1}{2} \overline{(h'_{ij})^2} + \frac{1}{2} \overline{(\nabla h_{ij})^2} \right\rangle \simeq \frac{m_P^2}{16a^2(\eta)} \left\langle \overline{(\nabla h_{ij})^2} \right\rangle, \quad (44)$$

where the overlines denote an average over time. This expression for the energy density can be rewritten in terms of the power spectrum of GWs as follows

$$\rho_{\text{GW}}(\eta) = \int d \ln k \rho_{\text{GW}}(\eta, k), \quad (45)$$

$$\rho_{\text{GW}}(\eta, k) = \frac{m_P^2}{8} \left( \frac{k}{a(\eta)} \right)^2 \overline{\mathcal{P}_h(\eta, k)}. \quad (46)$$

We can then define the density parameter of GWs per logarithmic interval of  $k$ ,

$$\Omega_{\text{GW}}(\eta, k) = \frac{\rho_{\text{GW}}(\eta, k)}{\rho_{\text{cr}}(\eta)} = \frac{1}{24} \left( \frac{k}{\mathcal{H}(\eta)} \right)^2 \overline{\mathcal{P}_h(\eta, k)}. \quad (47)$$

The expression for the power spectrum that we have computed in the previous section holds only during the RD era. The energy density of GWs decays as radiation, so we can easily estimate the fraction of energy density of GWs in terms of the current energy density of radiation  $\Omega_{r,0}$  and  $\Omega_{\text{GW}}(\eta_f, k)$  at a generic time  $\eta_f$  during the RD era, before the SM degrees of freedom become non relativistic. Taking  $\eta_f$  at a time when the top quark is non relativistic, and assuming that there are no extra relativistic degrees of freedom on top of the SM value  $g_{*,f} = 106.75$ , the radiation density at  $\eta_f$  is related to its current value by the conservation of entropy:

$$c_g \equiv \frac{a_f^4 \rho_{r,f}}{a_0^4 \rho_{r,0}} = \frac{g_{*,f}}{g_{*,0}} \left( \frac{g_{*,0}}{g_{*,f}} \right)^{4/3} \approx 0.4. \quad (48)$$

We can then write the current energy density of GWs by rescaling it from  $\eta_f$  until today by  $a^{-4}$ :

$$\Omega_{\text{GW}}(\eta_0, k) = (c_g \Omega_{r,0}) \Omega_{\text{GW}}(\eta_f, k) = c_g \frac{\Omega_{r,0}}{24} \frac{k^2}{\mathcal{H}(\eta_f)^2} \overline{\mathcal{P}_h(\eta_f, k)}. \quad (49)$$

We can collect the results of Eqs. (43) and (49), plug  $\mathcal{H}(\eta_f) = 1/\eta_f$  (valid through RD until  $\eta_f$ ), and perform a simplification for the average over time justified by the fact that  $k\eta \gg 1$

$$\frac{\overline{\cos^2(k\eta)}}{\eta^2} \sim \frac{\overline{\sin^2(k\eta)}}{\eta^2} \sim \frac{1}{2} \frac{1}{\eta^2}, \quad \frac{\overline{\sin(2k\eta)}}{\eta^2} \sim 0. \quad (50)$$

We finally obtain the current energy density of GWs

$$\Omega_{\text{GW}}(\eta_0, k) = \frac{c_g \Omega_{r,0}}{972} \iint_{\mathcal{S}} dx dy \frac{x^2}{y^2} \left[ 1 - \frac{(1+x^2-y^2)^2}{4x^2} \right]^2 \mathcal{P}_\zeta(kx) \mathcal{P}_\zeta(ky) [\mathcal{I}_c(x, y)^2 + \mathcal{I}_s(x, y)^2]. \quad (51)$$

#### IV. BISPECTRUM OF GRAVITATIONAL WAVES

In this section we compute the bispectrum (three-point function) of GWs. Let us start from the solution (32) for GWs, and write the three-point function as

$$\begin{aligned} \langle h^r(\eta, \mathbf{k}_1) h^s(\eta, \mathbf{k}_2) h^t(\eta, \mathbf{k}_3) \rangle &= \left(\frac{4}{9}\right)^3 \int \frac{d^3 p_1}{(2\pi)^3} \int \frac{d^3 p_2}{(2\pi)^3} \int \frac{d^3 p_3}{(2\pi)^3} \frac{1}{k_1^3 k_2^3 k_3^3 \eta^3} e^r(\mathbf{k}_1, \mathbf{p}_1) e^s(\mathbf{k}_2, \mathbf{p}_2) e^t(\mathbf{k}_3, \mathbf{p}_3) \\ &\cdot \left\langle \zeta(\mathbf{p}_1) \zeta(\mathbf{k}_1 - \mathbf{p}_1) \zeta(\mathbf{p}_2) \zeta(\mathbf{k}_2 - \mathbf{p}_2) \zeta(\mathbf{p}_3) \zeta(\mathbf{k}_3 - \mathbf{p}_3) \right\rangle [\cos(k_1 \eta) \mathcal{I}_c(x_1, y_1) + \sin(k_1 \eta) \mathcal{I}_s(x_1, y_1)] \\ &\cdot [\cos(k_2 \eta) \mathcal{I}_c(x_2, y_2) + \sin(k_2 \eta) \mathcal{I}_s(x_2, y_2)] [\cos(k_3 \eta) \mathcal{I}_c(x_3, y_3) + \sin(k_3 \eta) \mathcal{I}_s(x_3, y_3)], \quad (52) \end{aligned}$$

where  $x_i = p_i/k_i$  and  $y_i = |\mathbf{k}_i - \mathbf{p}_i|/k_i$ . The details of the calculation of the six-point function of the curvature perturbation  $\zeta$  are given in Appendix B. We have eight possible contractions for  $\mathbf{k}_i \neq 0$  that yield the same contribution to the bispectrum. We can evaluate the three-point function for any of these configurations and multiply by eight the result. The three-point function (52) becomes then (we understand that  $\mathbf{p}_2 = \mathbf{p}_1 - \mathbf{k}_1$ ,  $\mathbf{p}_3 = \mathbf{p}_1 + \mathbf{k}_3$ , and  $y_1 = x_2$ ,  $y_2 = x_3$ ,  $y_3 = x_1$ ):

$$\begin{aligned} \langle h^r(\eta, \mathbf{k}_1) h^s(\eta, \mathbf{k}_2) h^t(\eta, \mathbf{k}_3) \rangle &= (2\pi)^3 \delta^{(3)}(\mathbf{k}_1 + \mathbf{k}_2 + \mathbf{k}_3) 8 \left(\frac{4}{9}\right)^3 \pi^3 \int d^3 p_1 \frac{1}{k_1^3 k_2^3 k_3^3 \eta^3} \\ &\cdot e^r(\mathbf{k}_1, \mathbf{p}_1) e^s(\mathbf{k}_2, \mathbf{p}_2) e^t(\mathbf{k}_3, \mathbf{p}_3) \frac{\mathcal{P}_\zeta(p_1)}{p_1^3} \frac{\mathcal{P}_\zeta(p_2)}{p_2^3} \frac{\mathcal{P}_\zeta(p_3)}{p_3^3} \left[ \cos(k_1 \eta) \mathcal{I}_c\left(\frac{p_1}{k_1}, \frac{p_2}{k_1}\right) + \sin(k_1 \eta) \mathcal{I}_s\left(\frac{p_1}{k_1}, \frac{p_2}{k_1}\right) \right] \\ &\cdot \left[ \cos(k_2 \eta) \mathcal{I}_c\left(\frac{p_2}{k_2}, \frac{p_3}{k_2}\right) + \sin(k_2 \eta) \mathcal{I}_s\left(\frac{p_2}{k_2}, \frac{p_3}{k_2}\right) \right] \left[ \cos(k_3 \eta) \mathcal{I}_c\left(\frac{p_3}{k_3}, \frac{p_1}{k_3}\right) + \sin(k_3 \eta) \mathcal{I}_s\left(\frac{p_3}{k_3}, \frac{p_1}{k_3}\right) \right]. \quad (53) \end{aligned}$$

The polarisation tensors defined in Eq. (28) involve the angles  $\theta_i$ ,  $\phi_i$  (shown in Fig. 5 for  $i = 1$ ) which identify  $\mathbf{p}_i$  in spherical coordinates around the axis  $\mathbf{k}_i$ .

With reference to Fig. 5, the vectors  $\mathbf{k}_i$  in blue are given and we can choose a reference frame such that

$$\mathbf{k}_1 = (k_{1x}, k_{1y}, 0), \quad \mathbf{k}_2 = (k_{2x}, k_{2y}, 0), \quad \mathbf{k}_3 = (-k_3, 0, 0); \quad (54)$$

the quantities  $\ell$ ,  $r$ , and  $\alpha$  in green are a convenient choice of cylindrical coordinates as integration variables,

$$\int d^3 p_1 \longrightarrow \int_{-\infty}^{+\infty} d\ell \int_0^{+\infty} r dr \int_0^{2\pi} d\alpha; \quad (55)$$

the quantities marked in red give the expressions to plug in Eq. (53),

$$\begin{aligned} \mathbf{p}_1 &= (r \cos \alpha, r \sin \alpha, \ell), \quad \mathbf{p}_2 = (-k_{1x} + r \cos \alpha, -k_{1y} + r \sin \alpha, \ell), \quad \mathbf{p}_3 = (-k_3 + r \cos \alpha, r \sin \alpha, \ell), \\ p_i^2 \sin^2 \theta_i &= p_i^2 - \frac{|\mathbf{p}_i \cdot \mathbf{k}_i|^2}{k_i^2}, \quad \sin \phi_i = \frac{\ell k_i}{|\mathbf{p}_i \times \mathbf{k}_i|}. \quad (56) \end{aligned}$$

Eqs. (53), (28), and (33), with the replacements listed in (54), (55), (56), contain all the ingredients for the numerical calculation of the bispectrum of GWs.

Out of the eight possible polarisations ( $r, s, t$ ) of the three-point function, four of them vanish due to parity arguments applied to the polarisation tensors, in analogy to what happens for the two-point function, see Eq. (40). Among the terms contained in Eq. (53), the only ones which are odd under the parity transformation  $\ell \rightarrow -\ell$  (that is, a parity transformation with respect to the plane containing  $\mathbf{k}_1, \mathbf{k}_2, \mathbf{k}_3$ ) are the polarisation tensors  $e^\times$ , and all other terms are even. This implies that the only four non-vanishing polarisation combinations for the three-point functions are

$$(+++), \quad (+\times\times), \quad (\times+\times), \quad (\times\times+). \quad (57)$$

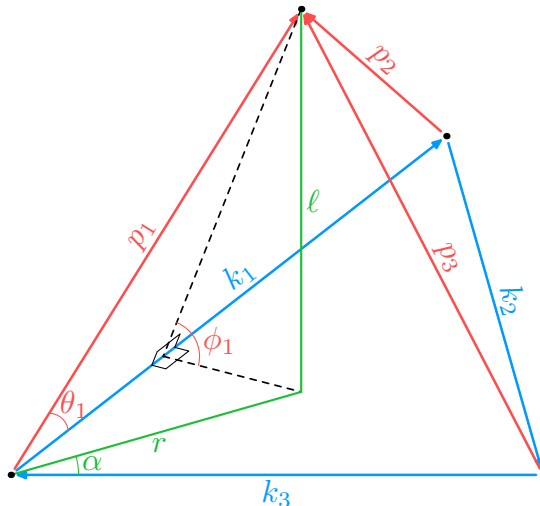


FIG. 5: Geometrical configuration for the contraction (i) of the 6-point function of  $\zeta$  written in Eq. (B.5).

## V. NUMERICAL RESULTS FOR THE ENERGY DENSITY AND BISPECTRUM OF GWS

### Energy density of GWs

We devote this section to the results of the numerical integration for the scalar power spectra  $\mathcal{P}_\zeta(k)$  obtained for a few illustrative cases of the mechanism discussed in [11] and summarised in the Introduction. We rewrite for convenience the energy density of GWs of Eq. (51) in terms of the variables  $(d, s)$  defined in Eq. (35) as

$$\Omega_{\text{GW}}(\eta_0, k) = \frac{c_g \Omega_{r,0}}{36} \int_0^{\frac{1}{\sqrt{3}}} dd \int_{\frac{1}{\sqrt{3}}}^\infty ds \left[ \frac{(d^2 - 1/3)(s^2 - 1/3)}{s^2 - d^2} \right]^2 \mathcal{P}_\zeta \left( \frac{k\sqrt{3}}{2}(s+d) \right) \mathcal{P}_\zeta \left( \frac{k\sqrt{3}}{2}(s-d) \right) [\mathcal{I}_c(d, s)^2 + \mathcal{I}_s(d, s)^2], \quad (58)$$

where the functions  $\mathcal{I}_c, \mathcal{I}_s$  are defined in (33) and are plotted in Figs. 3 and 4.

We consider the running of the quartic Higgs coupling  $\lambda$  for some sample points in the parameter space  $(m_{\text{top}}, m_{\text{Higgs}})$  denoted by the number of standard deviations from the measured central values. We have taken the current LHC combination  $m_{\text{Higgs}} = 125.09 \pm 0.24$  GeV [27] and  $m_{\text{top}} = 172.47 \pm 0.5$  GeV [28]. The corresponding running of the quartic Higgs coupling  $\lambda$  is shown in Fig. 6.

Each of these points defines therefore a different Higgs potential, for which we run an evolution of the Higgs field completely analogous to what was described in Ref. [11], by keeping a fixed Hubble rate  $H = 10^{12}$  GeV. This evolution leads to the creation of PBH during the radiation dominated era, with a peak in the mass function for scales of the order of  $k_*$ , the mode that leaves the Hubble radius at the time  $t_*$  when the classical evolution of the Higgs field starts, as described in the Introduction. The corresponding  $\mathcal{P}_\zeta$  has basically the same shape in all these cases, and what changes is the reference scale  $k_*$  for the enhancement of the power spectrum as we show in Fig. 7.<sup>2</sup>

The final result for the power spectra of GW is shown in Fig. 8, together with the comparison with the projected sensitivity of proposed future experiments. The sensitivity curve for LISA is estimated on the basis of the proposal [29]: the proposed design (4y, 2.5 Gm of length, 6 links) is expected to yield a sensitivity in between the ones dubbed C1 and C2 in Ref. [30]<sup>3</sup>. We also include the projected design sensitivity for Advanced LIGO + Virgo from Ref. [31], the estimated sensitivity for the proposed Einstein Telescope (ET) [32], and the estimated reach for the 5-years program of MAGIS-100 at FERMILAB [33].

The GW power spectra are shown for different combinations of the values of the Higgs and top masses where the symbols  $m_{\text{Higgs}}^{(\pm n\sigma)}$  and  $m_{\text{top}}^{(\pm n\sigma)}$  indicate their values  $\pm n\sigma$  away from their central values. A GW power spectrum for values of the Higgs boson mass  $m_{\text{Higgs}} = 125.09$  GeV (the current central value) and  $m_{\text{top}} = 171.47$  GeV, is well

<sup>2</sup> If the same mechanism is supposed to give rise to PBHs, then these power spectra yield a final abundance  $\Omega_{\text{PBH}}/\Omega_{\text{CDM}}$  ranging between  $10^{-3}$  and  $10^{-1}$  when no accretion is included [11].

<sup>3</sup> We thank G. Nardini for clarifying discussions about this point.

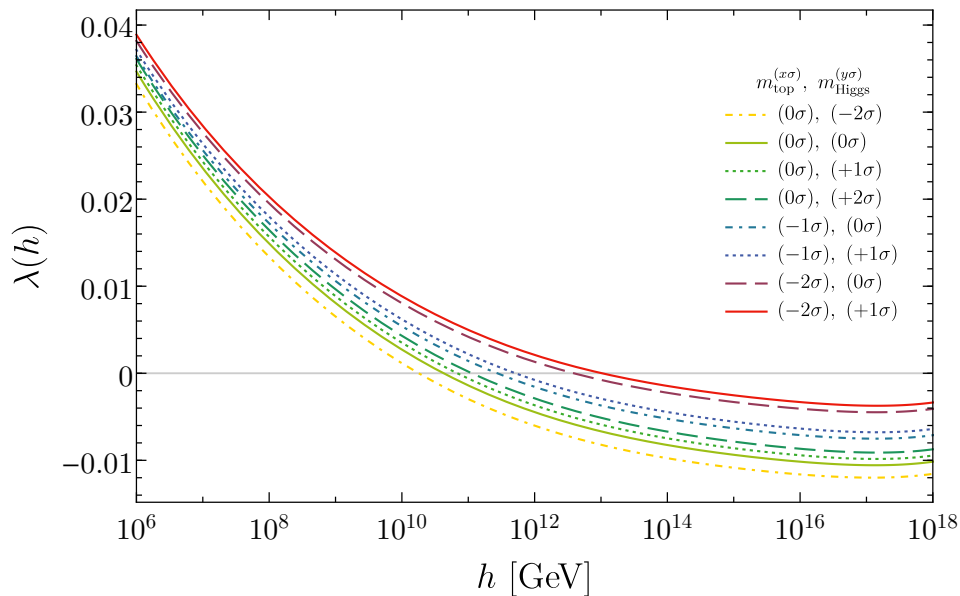


**FIG. 6:** Running of the quartic Higgs coupling  $\lambda$  for the following Higgs and top masses:  $m_{\text{Higgs}} = 125.09 \pm 0.24$  GeV and  $m_{\text{top}} = 172.47 \pm 0.5$  GeV.

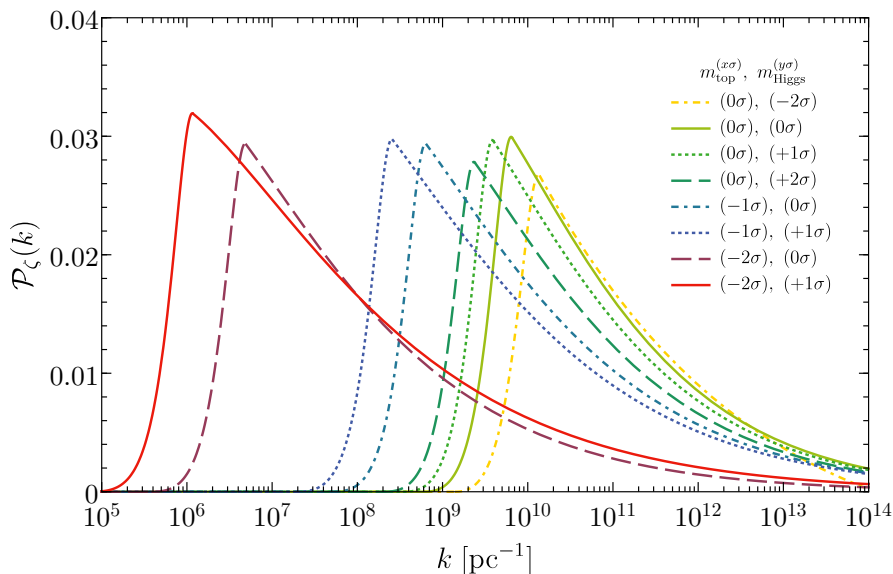


**FIG. 7:** The power spectrum of the comoving curvature perturbation during the radiation phase obtained in Ref. [11] for the following Higgs and top masses:  $m_{\text{Higgs}} = 125.09 \pm 0.24$  GeV and  $m_{\text{top}} = 172.47 \pm 0.5$  GeV.

within the reach of LISA. To relate the amount of GWs and the PBH abundance at formation following the proposal in Ref. [11], one can use the relation  $M_{\text{PBH}} \simeq 50M_{\odot}(10^{-9}\text{Hz}/f)^2$ . In Fig. 8, we have used that relation to translate the frequencies of the GW signal in terms of the peak mass of the PBH distribution.

One fundamental information to be drawn from Fig. 8 is that the frequency at the peak depends in a sensitive way on the Higgs and top masses, ranging from  $10^{-2}$  to about 10 Hz, see Table I. Therefore, according to the Higgs and top masses, the signal falls either within the LISA or the ET and Advanced-Ligo sensitivity curves. This implies that a detected signal can be cross-checked with the information obtained through colliders, thus either confirming or ruling out its Standard Model origin.

We draw the attention of the reader that our results for the GW power spectra in Fig. 8 are sensitive to the value

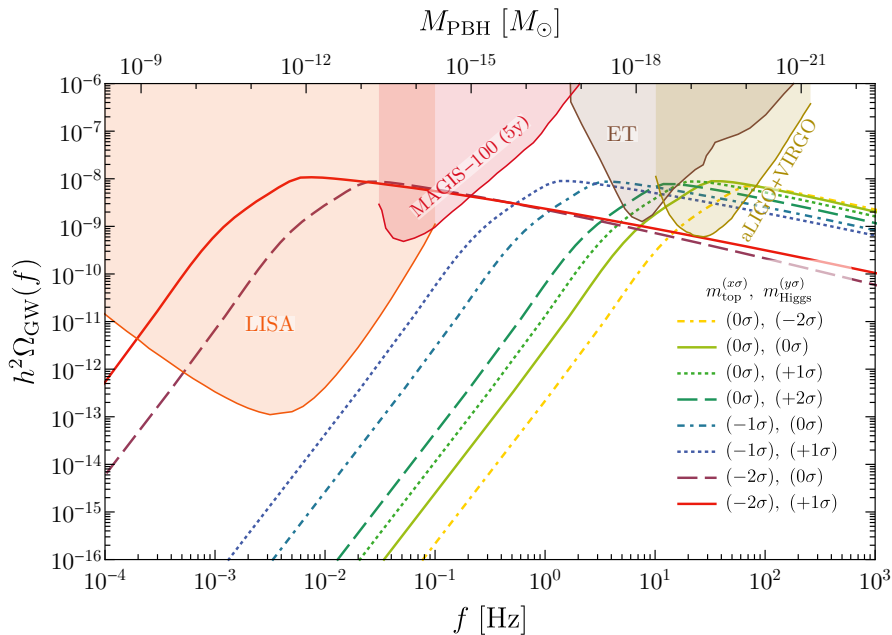


**FIG. 8:** Power spectra of GWs for the scalar power spectra generated by the mechanism discussed in Ref. [11], compared with the estimated sensitivities for LISA, the Einstein Telescope, MAGIS-100, and the design sensitivity of Advanced LIGO + Virgo. The Higgs and top mass values are  $m_{\text{Higgs}} = 125.09 \pm 0.24$  GeV and  $m_{\text{top}} = 172.47 \pm 0.5$  GeV.

of the Higgs field at the beginning of its classical dynamics. A per mill change in such a value can lead to variations of the power spectrum of the curvature perturbation by (2 – 4) orders of magnitude. However, from Fig. 8 it is clear that we can still afford a change in  $\mathcal{P}_\zeta$  of three orders of magnitude.

### The spectral tilt of GWs at low and high frequencies

As we have mentioned in the introduction, the spectral tilt of the GW spectrum is a very interesting observable as GWs cover a large range of frequencies. For instance, writing the GW energy density as  $\Omega_{\text{GW}} = \Omega_{\text{GW}}^{\text{CMB}}(f/f_{\text{CMB}})^{n_T}$ , being  $n_T$  the spectral tilt and  $f_{\text{CMB}} \sim 7.7 \cdot 10^{-17}$  Hz the CMB frequency, a limit of  $n_T \lesssim 0.35$  can in principle be obtained for the best LISA configuration with six links, five million km arm length and a five year mission [4].

If the scalar power spectrum  $\mathcal{P}_\zeta(k)$  is vanishing or negligible for  $k$  smaller than some scale  $k_*$ , and approximately constant for  $k > k_*$  as in our case, then at small  $k$  we have  $\Omega_{\text{GW}} \sim k^3$ . Indeed, in this case  $\mathcal{P}_\zeta(kx)$  in Eq. (58) for  $k \ll k_*$  selects  $s \gtrsim 1/k$  in the integral over  $s$ , so that the tail at high  $s$  of  $\mathcal{I}_{c,s}(d, s)$  is peaked up and it goes as  $1/s^2$  (see Fig. 4). The resulting overall integral is therefore of order

$$\int_{1/k} \frac{ds}{s^4} \sim k^3. \quad (59)$$

As for the spectral tilt at  $k \gg k_*$ , the integral over  $s$  in Eq. (58) is peaked at  $s \sim \sqrt{3}$  due to the spike in  $\mathcal{I}_{c,s}(d, s)$  (see Fig. 4) and the dependence on  $k$  comes from  $\mathcal{P}_\zeta(kx)\mathcal{P}_\zeta(k(\sqrt{3}-x))$  which has a spectral tilt equal roughly to twice the spectral index of  $\mathcal{P}_\zeta$ . In our case,  $\mathcal{P}_\zeta(k) \sim k^{-0.35}$  and  $\Omega_{\text{GW}}(k)$  turns out to go as  $\sim k^{-0.6}$ . For a narrow scalar power spectrum  $\mathcal{P}_\zeta(k)$ , we would expect by similar arguments a spectral index  $\sim +2$  at small  $k$  and a quite sharp cutoff at high  $k$ .

The final parametrisation of the GW spectrum induced by the Higgs fluctuations is therefore

$$\Omega_{\text{GW}}(f) \simeq 3 \cdot 10^{-8} \left( \frac{f}{f_*} \right)^{n_T} \quad \text{with} \quad n_T = \begin{cases} 3 & \text{for } f < f_*, \\ -0.6 & \text{for } f > f_*. \end{cases} \quad (60)$$

The values of  $f_*$  for the cases we consider are listed in Table I. The parametrisation of Eq. (60) is useful to deduce its detectability by LISA. The investigation of a generic GW background whose energy density is parametrised as

$m_{\text{top}}^{(x\sigma)}$	$m_{\text{Higgs}}^{(y\sigma)}$	$f_*$ (Hz)
(0 $\sigma$ )	(-2 $\sigma$ )	40.0
(0 $\sigma$ )	(0 $\sigma$ )	21.8
(0 $\sigma$ )	(+1 $\sigma$ )	13.0
(0 $\sigma$ )	(+2 $\sigma$ )	7.74
(-1 $\sigma$ )	(0 $\sigma$ )	2.02
(-1 $\sigma$ )	(+1 $\sigma$ )	0.80
(-2 $\sigma$ )	(0 $\sigma$ )	0.015
(-2 $\sigma$ )	(+1 $\sigma$ )	0.0038

**TABLE I:** Values of  $f_*$  defined in Eq. (60) for each of the cases considered in Fig. 8.

$\Omega_{\text{GW}}(f) = A(f/f_*)^{n_T}$  can be found in Ref. [4] where it was imposed that the signal-to-noise ratio is larger than 10, see Fig. 2 of Ref. [4]. It seems that for the case of Higgs mass  $m_{\text{Higgs}} = 125.09$  GeV and  $m_{\text{top}} = 171.47$  GeV not only the amplitude of the gravitational waves from Higgs perturbations, but also its spectral index can be measured with accuracy, opening the possibility of a full identification of the underlying mechanism.

Were GWs found, the value of the frequency  $f_*$  would allow to identify the approximate position of the instability scale  $\Lambda_I$  of the Higgs potential, defined by  $V(\Lambda_I) = 0$ . The instability scale  $\Lambda_I$  can be identified by the relation

$$\Lambda_I \simeq 3 \cdot 10^{11} \left( \frac{f_*}{\text{Hz}} \right)^{-0.65} \text{ GeV}. \quad (61)$$

We stress that this relation is robust in the sense that the frequency changes very little even when the overall amplitude of the GW signal decreases due to a variation of the initial condition of the classical Higgs field. It is remarkable that a measurement of the frequency of the GW signal can be directly related to such a high energy scale.

### The three-point correlator of GWs and its consistency relations

In this subsection we present our findings for the three-point correlator of the GWs. As mentioned in the introduction, the community has already started discussing the detectability of such non-Gaussian signal at interferometers [34]. The ultimate reason for measuring the GW bispectrum is to exploit the correspondence between the three-point and the two-point correlators in order to discriminate the different mechanisms which give rise to a GW signal hopefully measured by LISA. Unfortunately, such a non-Gaussian signal seems not an observable quantity with a GW detector, which unavoidably detects the sum of the GW signals from all patches of the sky. The sum of all these signals, independently from their primordial correlation, results as a Gaussian signal by virtue of the Central Limit Theorem (see [18] for a detailed discussion).

We define the bispectrum  $B_h^{rst}(\mathbf{k}_1, \mathbf{k}_2, \mathbf{k}_3)$  (the temporal dependence on  $\eta$  is understood) as

$$\langle h^r(\eta, \mathbf{k}_1) h^s(\eta, \mathbf{k}_2) h^t(\eta, \mathbf{k}_3) \rangle \equiv (2\pi)^3 \delta^{(3)}(\mathbf{k}_1 + \mathbf{k}_2 + \mathbf{k}_3) B_h^{rst}(\mathbf{k}_1, \mathbf{k}_2, \mathbf{k}_3). \quad (62)$$

We also define a dimensionless normalised shape  $S_h^{rst}(\mathbf{k}_1, \mathbf{k}_2, \mathbf{k}_3)$  in order to cancel the time scaling of GWs as  $1/\eta$  [see Eq. (32)]:

$$S_h^{rst}(\mathbf{k}_1, \mathbf{k}_2, \mathbf{k}_3) = k_1^2 k_2^2 k_3^2 \frac{B_h^{rst}(\mathbf{k}_1, \mathbf{k}_2, \mathbf{k}_3)}{\sqrt{\mathcal{P}_h(k_1) \mathcal{P}_h(k_2) \mathcal{P}_h(k_3)}}, \quad (63)$$

where  $\mathcal{P}_h(k)$  is the dimensionless power spectrum defined in Eq. (42). As for the oscillatory behaviour of the two- and three-point functions, we consider their envelope in time. This simplification is not physically adequate when considering the three-point function measured by a GW detector, given that the overall phase of would depend on the direction of propagation of the incoming wave and is crucial when assessing the non-Gaussianity of the signal. In the present discussion, it is motivated by our interest in the amplitude of the primordial bispectrum which could be measurable in principle on a constant time hypersurface. We replace then the oscillating function in squared brackets in the solution (32) by its envelope

$$\mathcal{I}_c(x, y) \cos(k\eta) + \mathcal{I}_s(x, y) \sin(k\eta) \rightarrow \sqrt{\mathcal{I}_c(x, y)^2 + \mathcal{I}_s(x, y)^2}, \quad (64)$$

both for  $B_h$  and  $\mathcal{P}_h$  in Eq. (63).

We show the numerical results for the bispectrum by fixing the value of  $k_3$  and by ordering the momenta as  $k_1 \leq k_2 \leq k_3$ . Figs. 9 and 10 show contours of  $S_h(\mathbf{k}_1, \mathbf{k}_2, \mathbf{k}_3)$  in the plane  $(k_1/k_3, k_2/k_3)$  for two values of  $k_3$  close to the maximum of  $\mathcal{P}_\zeta(k)$  (shown in Fig. 7). We choose the case  $(m_{\text{top}}^{(-2\sigma)}, m_{\text{higgs}}^{(0\sigma)})$ , as it falls into the window detectable by LISA, but we notice that the result is identical for the other cases, given that the shape of the power spectrum is identical, up to a rescaling of the momenta  $(k_1, k_2, k_3)$ . We also notice that the normalised shape defined in Eq. (63) is invariant under rescaling of the scalar power spectrum  $\mathcal{P}_\zeta(k)$ . In Fig. 9, together with the separate plots for each polarisation, we also show their sum in the lower two plots, both with contours and with a three-dimensional plot.

From these numerical results we observe several features. First of all, we remind the reader that there are traditionally several configurations one can analyse: the local one where the signal is peaked for squeezed configurations  $k_1 \ll k_2 \simeq k_3$ ; the equilateral configuration peaks for equilateral configurations  $k_1 \simeq k_2 \simeq k_3$  for which the strongest correlations between fluctuation modes happen when they cross the horizon approximately at the same time; the folded configuration for which the signal is boosted for  $k_1 + k_2 \simeq k_3$ ; and finally the orthogonal configuration ( $k_1 \simeq k_2$ ) which creates a signal with a positive peak at the equilateral configuration and a negative peak at the folded configuration.

The signal is peaked in the equilateral configuration. This does not come as a surprise as the GWs are generated at Hubble crossing and the source depends on spatial gradients of the comoving curvature perturbations and this tends to enhance the signal when the scales involved are not too different. As a rule of thumb we can propose the following consistency relation for the largest signals

$$\boxed{\begin{aligned} S_h^{+++} &= \mathcal{O}(-10^3) \text{ for equilateral configurations,} \\ S_h^{+\times\times} &= \mathcal{O}(-10^4) \text{ for equilateral configurations.} \end{aligned}} \quad (65)$$

As for the signal summed for all the polarizations, the results are presented in the lower plot of Fig. 9. From it we can estimate

$$\boxed{\sum_{\text{pol}} S_h = \mathcal{O}(-3 \cdot 10^4) \text{ for equilateral configurations.}} \quad (66)$$

## VI. CONCLUSIONS

In this paper we have characterized the GW signal possibly originated by physics of the Standard Model and its inherent instability scale appearing in the Higgs scalar sector. In this sense, GW physics allows a test, albeit indirect, of the behaviour of the Standard Model at large field values. The source of the GWs is generated by the Higgs perturbations created during a primordial epoch of inflation and amplified during the phase in which the Higgs probes the unstable part of the potential.

The energy density  $\Omega_{\text{GW}}$  can be as large as  $10^{-8}$  and therefore measurable either by LISA or by the ET and Advanced-Ligo, the amplitude being sensitive to the initial conditions of the Higgs classical dynamics. Which experiment turns out to be relevant is dictated by the frequency at the peak of the signal, which in turn depends on the Higgs and top masses. This is indeed a bonus. The more knowledge from collider physics is collected on these masses, the more one could confirm or disprove the hypothesis that these GWs come from Standard Model physics.

We have also characterized the signal in terms of its spectral index as well as three-point correlator. This non-Gaussian feature of the signal would not be observable unfortunately in a GW detector, which could measure only the sum of signals from many patches in the sky, whose phases would have been further decorrelated by the propagation in the inhomogeneous background. Therefore a detection of both a two- and three-point function of a signal would indicate its non-primordial origin.

We close with some comments. The mechanism described in this paper makes use of the fact that we identify our observed Universe as one of those regions which have been thermally saved during the reheating stage following inflation after the Higgs has probed the unstable part of its potential during inflation. The choice of the parameters might therefore seem fine-tuned. However, anthropic arguments come to the rescue as the very same dynamics might create the dark matter of the Universe under the form of PBHs [11]. Put in other words, if the dark matter has to be ascribed to the Standard Model, then one should also detect the corresponding GW signal.

### Note added

In this paper we have calculated the amount of gravitational waves induced by the Higgs perturbations generated thanks to the Higgs vacuum instability. This result is independent from the possibility that the same Higgs perturbations



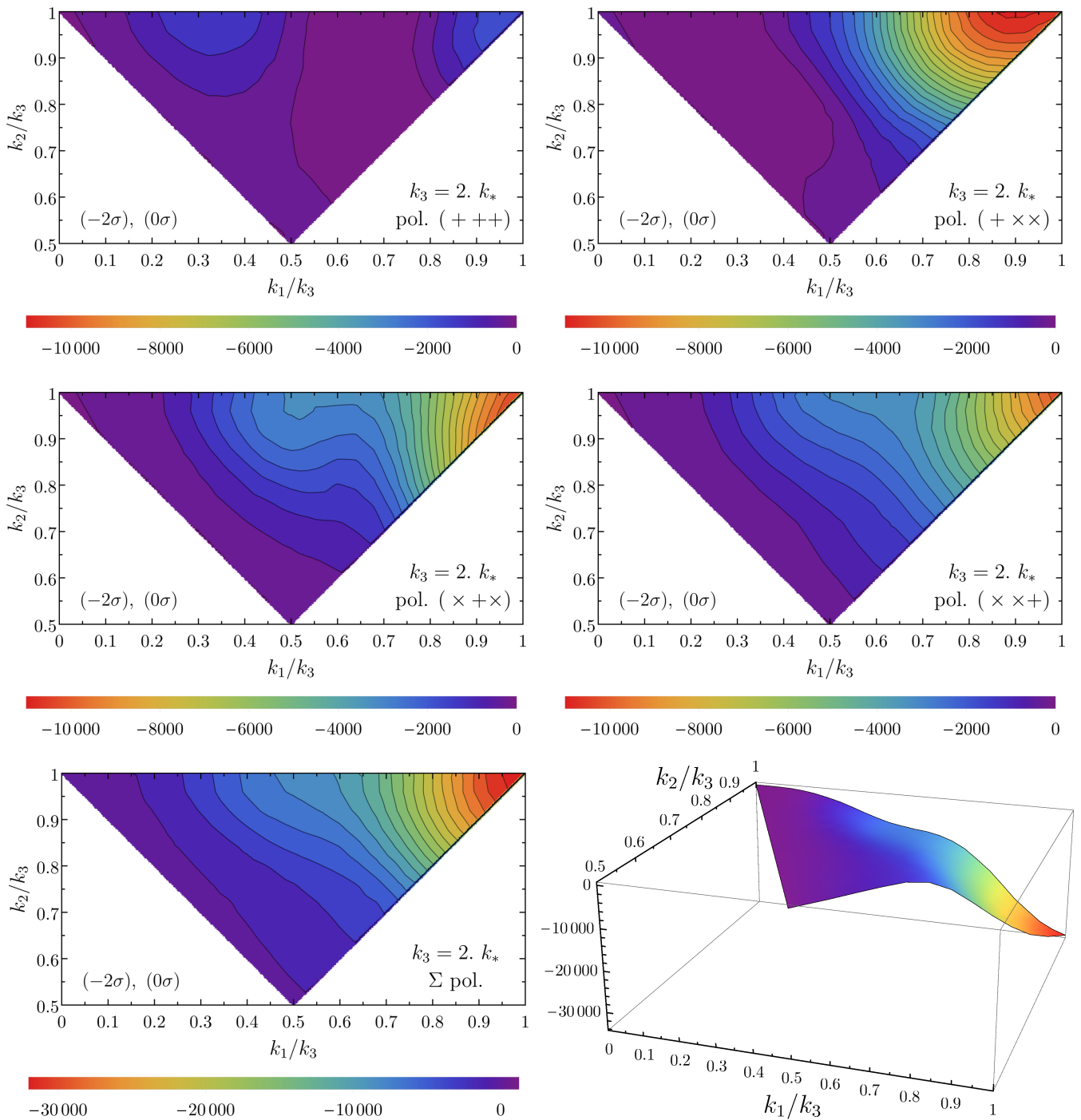


**FIG. 9:** Normalised shapes of GWs [defined in Eq. (63)] for the spectrum in the case  $(m_{\text{top}}^{(-2\sigma)}, m_{\text{higgs}}^{(0\sigma)})$ . Here  $k_3$  is fixed to be  $2k_*$ , corresponding to 0.04 Hz. The upper four plots show the four non-vanishing polarisations listed in Eq. (57). The two plots at the bottom show the sum over all the polarisations.

are responsible for (a fraction of) the dark matter in the universe. Even assuming that the latter comes from physics beyond the Standard Model, the gravitational waves can be a cosmological signature of the Higgs vacuum instability. More comments on the PBH issue and fine-tuning can be found in Ref. [35].

### Acknowledgements

We thank Nicola Bartolo and Germano Nardini for comments and for many useful discussions on LISA. We thank

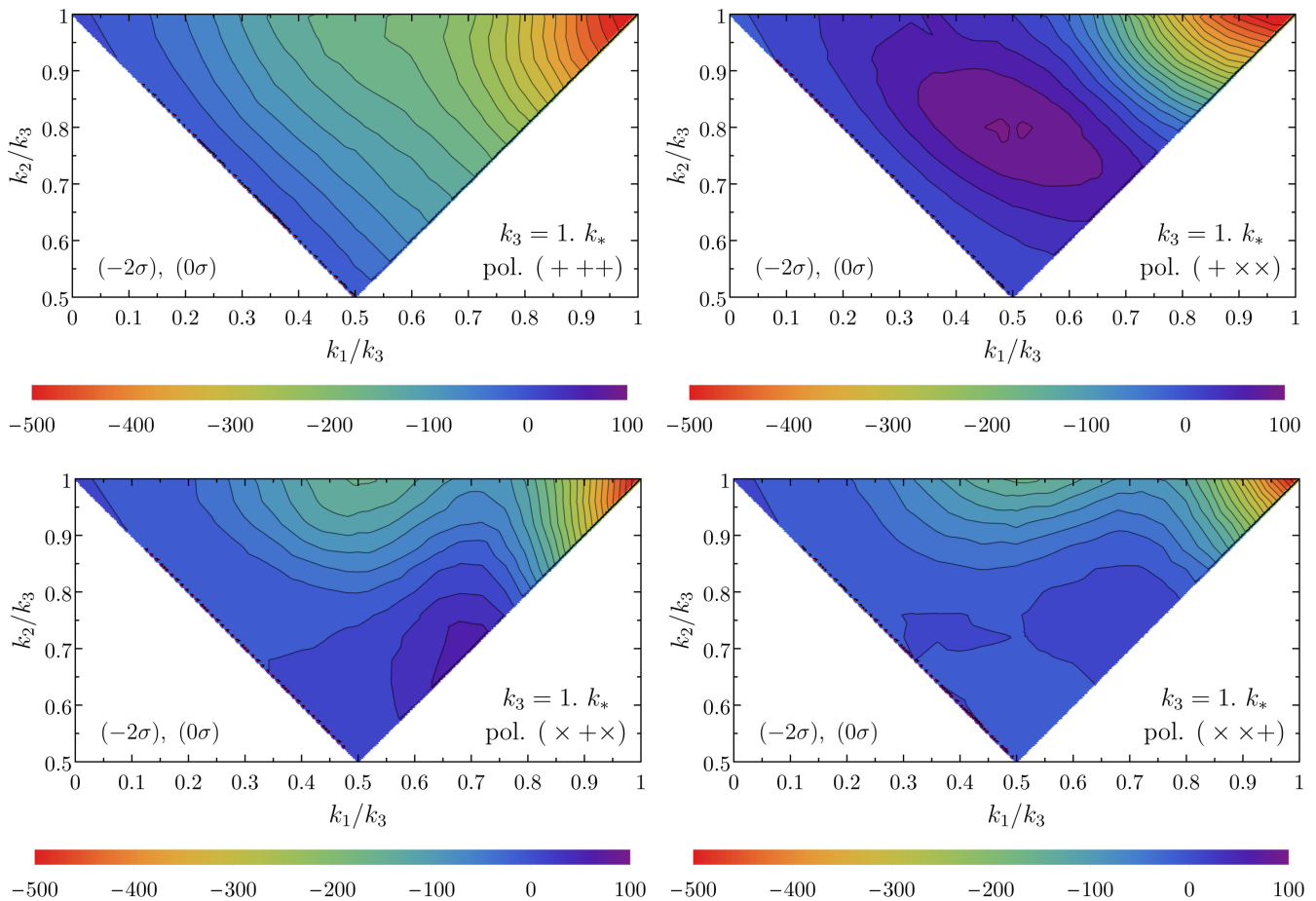


FIG. 10: Same as Fig. 9, for  $k_3 = k_*$ , corresponding to 0.02 Hz.

also Kazunori Kohri and Takahiro Terada for useful discussions about the comparison of their results, and Subodh Patil for useful correspondence. A.R. and D.R. are supported by the Swiss National Science Foundation (SNSF), project *Investigating the Nature of Dark Matter*, project number: 200020-159223. The work of J.R.E. has been partly supported by the ERC grant 669668 – NEO-NAT – ERC-AdG-2014, the Spanish Ministry MINECO under grants 2016-78022-P and FPA2014-55613-P, the Severo Ochoa excellence program of MINECO (grants SEV-2016-0588 and SEV-2016-0597) and by the Generalitat de Catalunya grant 2014-SGR-1450.

### Appendix A: Dynamics of the Higgs hitting the pole

To understand Eq. (6) one solves the equation

$$\ddot{h}_c - \lambda h_c^3 = 0, \quad (\text{A.1})$$

Taking the initial conditions  $h_c(0) = h_0$  and  $\dot{h}_c(0) = \dot{h}_0$ , and using the fact that there is an integral of motion

$$\frac{1}{2}\dot{h}_c^2 - \frac{\lambda}{4}h_c^4 = -E = \frac{1}{2}\dot{h}_0^2 - \frac{\lambda}{4}h_0^4, \quad (\text{A.2})$$

one finds the solution

$$h_c(t) = h_0 \alpha_0 \operatorname{cn} \left( i\sqrt{\lambda} h_0 \alpha_0 t + \operatorname{cn}^{-1}(1/\alpha_0, 1/2), 1/2 \right), \quad (\text{A.3})$$

where  $\text{cn}(z, k)$  is one of the Jacobian elliptic functions and

$$\alpha_0 \equiv \left(1 - \frac{2h_0^2}{\lambda h_0^4}\right)^{1/4}. \quad (\text{A.4})$$

The function  $\text{cn}(ix, 1/2)$  has poles at  $x = K(1/2)$  with residue  $-i\sqrt{2}$ , where

$$K(k) = \int_0^{\pi/2} \frac{d\theta}{\sqrt{1 - k \sin^2 \theta}}. \quad (\text{A.5})$$

Around the pole the classical value of the Higgs can therefore be approximated by Eq. (6) with

$$t_p = \frac{1}{\sqrt{\lambda} h_0 \alpha_0} [K(1/2) + i \text{cn}^{-1}(1/\alpha_0, 1/2)]. \quad (\text{A.6})$$

## Appendix B: Four and Six-Point Functions of the Curvature Perturbation

### Four-point function of the curvature perturbation

The four-point function of the curvature perturbation  $\zeta$  in the first line of (36) has two possible non-vanishing contractions for  $\mathbf{k}_1, \mathbf{k}_2 \neq 0$

$$\begin{aligned} (i) \quad & \left\langle \zeta(\mathbf{p}_1) \zeta(\mathbf{k}_1 - \mathbf{p}_1) \zeta(\mathbf{p}_2) \zeta(\mathbf{k}_2 - \mathbf{p}_2) \right\rangle \\ (ii) \quad & \left\langle \zeta(\mathbf{p}_1) \zeta(\mathbf{k}_1 - \mathbf{p}_1) \zeta(\mathbf{p}_2) \zeta(\mathbf{k}_2 - \mathbf{p}_2) \right\rangle \quad (\text{obtained from (i) by } \mathbf{p}_2 \rightarrow (\mathbf{k}_2 - \mathbf{p}_2)) \end{aligned} \quad (\text{B.1})$$

The two contractions (i), (ii) correspond to the configuration of momenta shown in Fig. 11. The sum of the contractions

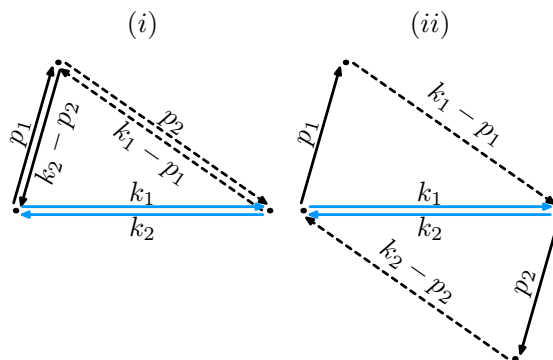


FIG. 11: Geometrical configurations for the non-vanishing contractions of the two-point function listed in Eq. (B.1).

(i) and (ii) gives

$$\begin{aligned} & \left\langle \zeta(\mathbf{p}_1) \zeta(\mathbf{k}_1 - \mathbf{p}_1) \zeta(\mathbf{p}_2) \zeta(\mathbf{k}_2 - \mathbf{p}_2) \right\rangle = \\ & = (2\pi)^6 \delta^{(3)}(\mathbf{k}_1 + \mathbf{k}_2) \left[ \delta^{(3)}(\mathbf{k}_2 + \mathbf{p}_1 - \mathbf{p}_2) + \delta^{(3)}(\mathbf{p}_1 + \mathbf{p}_2) \right] \frac{2\pi^2}{p_1^3} \frac{2\pi^2}{|\mathbf{k}_1 - \mathbf{p}_1|^3} \mathcal{P}_\zeta(p_1) \mathcal{P}_\zeta(|\mathbf{k}_1 - \mathbf{p}_1|). \end{aligned} \quad (\text{B.2})$$

The two contributions give the same result, given that they correspond to each other up to a shift  $\mathbf{p}_2 \rightarrow (\mathbf{k}_2 - \mathbf{p}_2)$ , which is a symmetry of Eq. (36).

To check the symmetry of the whole integral under the exchange of  $\mathbf{p}, \mathbf{k} - \mathbf{p}$ , it is important to observe that, for a generic function  $f$ ,

$$\int d^3 p e^{s,ij}(\mathbf{k}) p_i p_j f(\mathbf{k} - \mathbf{p}) f(\mathbf{p}) = \int d^3 \tilde{p} e^{s,ij}(\mathbf{k}) (k_i - \tilde{p}_i) (k_j - \tilde{p}_j) f(\tilde{\mathbf{p}}) f(\mathbf{k} - \tilde{\mathbf{p}}) = \int d^3 \tilde{p} e^{s,ij}(\mathbf{k}) \tilde{p}_i \tilde{p}_j f(\tilde{\mathbf{p}}) f(\mathbf{k} - \tilde{\mathbf{p}}), \quad (\text{B.3})$$

since  $e^{s,ij}(\mathbf{k})$  is transverse to  $\mathbf{k}$ .

We can evaluate then Eq. (36) for any of the two configurations, and multiply the final result by 2, to get Eq. (38) after integration over  $\mathbf{p}_2$  with a Dirac delta so that  $\mathbf{p}_2 = \mathbf{p}_1 - \mathbf{k}_1$ , and  $\mathbf{k}_2 = -\mathbf{k}_1$ .

### Six-point function of the curvature perturbation

To calculate the six-point function of  $\zeta$  that appears in (52) we have eight possible contractions for  $\mathbf{k}_i \neq 0$ , listed in Eq. (B.4). This total number of eight can be understood as the product of four choices for the contraction of  $\zeta(\mathbf{p}_1)$  times the number of contractions for the remaining four  $\zeta$ 's, that is two. All these contractions yield the same contribution to the bispectrum, thanks to the invariance of Eq. (52) under the exchange of the subscripts 1 and 2 and under  $\mathbf{p}_i \rightarrow \mathbf{k}_i - \mathbf{p}_i$ , as shown in Eq. (B.3) and (33).

$$\begin{aligned}
(i) & \left\langle \zeta(\mathbf{p}_1)\zeta(\mathbf{k}_1 - \mathbf{p}_1)\zeta(\mathbf{p}_2)\zeta(\mathbf{k}_2 - \mathbf{p}_2)\zeta(\mathbf{p}_3)\zeta(\mathbf{k}_3 - \mathbf{p}_3) \right\rangle & (B.4) \\
(ii) & \left\langle \zeta(\mathbf{p}_1)\zeta(\mathbf{k}_1 - \mathbf{p}_1)\zeta(\mathbf{p}_2)\zeta(\mathbf{k}_2 - \mathbf{p}_2)\zeta(\mathbf{p}_3)\zeta(\mathbf{k}_3 - \mathbf{p}_3) \right\rangle & (\text{obtained from (i) by } \mathbf{p}_1 \rightarrow (\mathbf{k}_1 - \mathbf{p}_1) ) \\
(iii) & \left\langle \zeta(\mathbf{p}_1)\zeta(\mathbf{k}_1 - \mathbf{p}_1)\zeta(\mathbf{p}_2)\zeta(\mathbf{k}_2 - \mathbf{p}_2)\zeta(\mathbf{p}_3)\zeta(\mathbf{k}_3 - \mathbf{p}_3) \right\rangle & (\text{obtained from (i) by } \mathbf{p}_3 \rightarrow (\mathbf{k}_3 - \mathbf{p}_3) ) \\
(iv) & \left\langle \zeta(\mathbf{p}_1)\zeta(\mathbf{k}_1 - \mathbf{p}_1)\zeta(\mathbf{p}_2)\zeta(\mathbf{k}_2 - \mathbf{p}_2)\zeta(\mathbf{p}_3)\zeta(\mathbf{k}_3 - \mathbf{p}_3) \right\rangle & (\text{obtained from (i) by } \mathbf{p}_2 \rightarrow (\mathbf{k}_2 - \mathbf{p}_2) ) \\
(v) & \left\langle \zeta(\mathbf{p}_1)\zeta(\mathbf{k}_1 - \mathbf{p}_1)\zeta(\mathbf{p}_2)\zeta(\mathbf{k}_2 - \mathbf{p}_2)\zeta(\mathbf{p}_3)\zeta(\mathbf{k}_3 - \mathbf{p}_3) \right\rangle & (\text{obtained from (i) by } 1 \leftrightarrow 2 ) \\
(vi) & \left\langle \zeta(\mathbf{p}_1)\zeta(\mathbf{k}_1 - \mathbf{p}_1)\zeta(\mathbf{p}_2)\zeta(\mathbf{k}_2 - \mathbf{p}_2)\zeta(\mathbf{p}_3)\zeta(\mathbf{k}_3 - \mathbf{p}_3) \right\rangle & (\text{obtained from (i) by } \mathbf{p}_1 \rightarrow (\mathbf{k}_1 - \mathbf{p}_1) \text{ and } 1 \leftrightarrow 2 ) \\
(vii) & \left\langle \zeta(\mathbf{p}_1)\zeta(\mathbf{k}_1 - \mathbf{p}_1)\zeta(\mathbf{p}_2)\zeta(\mathbf{k}_2 - \mathbf{p}_2)\zeta(\mathbf{p}_3)\zeta(\mathbf{k}_3 - \mathbf{p}_3) \right\rangle & (\text{obtained from (i) by } \mathbf{p}_3 \rightarrow (\mathbf{k}_3 - \mathbf{p}_3) \text{ and } 1 \leftrightarrow 2 ) \\
(viii) & \left\langle \zeta(\mathbf{p}_1)\zeta(\mathbf{k}_1 - \mathbf{p}_1)\zeta(\mathbf{p}_2)\zeta(\mathbf{k}_2 - \mathbf{p}_2)\zeta(\mathbf{p}_3)\zeta(\mathbf{k}_3 - \mathbf{p}_3) \right\rangle & (\text{obtained from (i) by } \mathbf{p}_2 \rightarrow (\mathbf{k}_2 - \mathbf{p}_2) \text{ and } 1 \leftrightarrow 2 )
\end{aligned}$$

In Fig. 12 we show the resulting geometrical configurations for the six momenta  $\mathbf{p}_i$ ,  $(\mathbf{k}_i - \mathbf{p}_i)$ , projected on the plane of the triangle formed by the  $\mathbf{k}_i$ . Notice indeed that all the contractions result in a common factor  $\delta^{(3)}(\mathbf{k}_1 + \mathbf{k}_2 + \mathbf{k}_3)$ . The labels of the vectors are printed only for the contraction (i) to facilitate the reading.

We can evaluate the three-point function for any of these configurations and multiply by eight the result. We choose the contraction (i), which is equal to

$$\begin{aligned}
& \left\langle \zeta(\mathbf{p}_1)\zeta(\mathbf{k}_1 - \mathbf{p}_1)\zeta(\mathbf{p}_2)\zeta(\mathbf{k}_2 - \mathbf{p}_2)\zeta(\mathbf{p}_3)\zeta(\mathbf{k}_3 - \mathbf{p}_3) \right\rangle = \\
& (2\pi)^9 \delta^{(3)}(\mathbf{k}_1 + \mathbf{k}_2 + \mathbf{k}_3) (2\pi^2)^3 \frac{\mathcal{P}_\zeta(p_1)}{p_1^3} \frac{\mathcal{P}_\zeta(p_2)}{p_2^3} \frac{\mathcal{P}_\zeta(p_3)}{p_3^3} \delta^{(3)}(\mathbf{p}_1 + \mathbf{k}_3 - \mathbf{p}_3) \delta^{(3)}(\mathbf{k}_1 - \mathbf{p}_1 + \mathbf{p}_2). \quad (B.5)
\end{aligned}$$

We then proceed to the integration of the three-point function over the conjugate momenta. The Dirac deltas in Eq. (B.5) fix the geometrical configuration of the six momenta  $\mathbf{k}_i$ ,  $\mathbf{p}_i$  as shown in Fig. 5. We can integrate over  $d^3p_2$  and  $d^3p_3$  in Eq. (52) with the last two Dirac deltas in (B.5). The result is (53) and the remaining integral in  $d^3p_1$  has to be evaluated numerically.

### Appendix C: The final curvature perturbation in the radiation phase

In this Appendix we follow the evolution of the perturbations during the reheating phase, which we consider for simplicity to be instantaneous (happening for instance in hybrid models in which a heavy waterfall field releases its vacuum energy providing a fast transition from inflation to radiation), and the subsequent radiation phase. To model the sudden transition from inflation to radiation one can imagine that the equations of motion of the Higgs and its perturbations possess a time-dependent term taking care of the fast appearance of the plasma correction to the potential under the form of the  $m_T^2 h^2$  term. By continuity,  $h_c(t_e) = h_c(t_{RH})$ ,  $\dot{h}_c(t_e) = \dot{h}_c(t_{RH})$ ,  $\delta h(t_e) = \delta h(t_{RH})$ ,

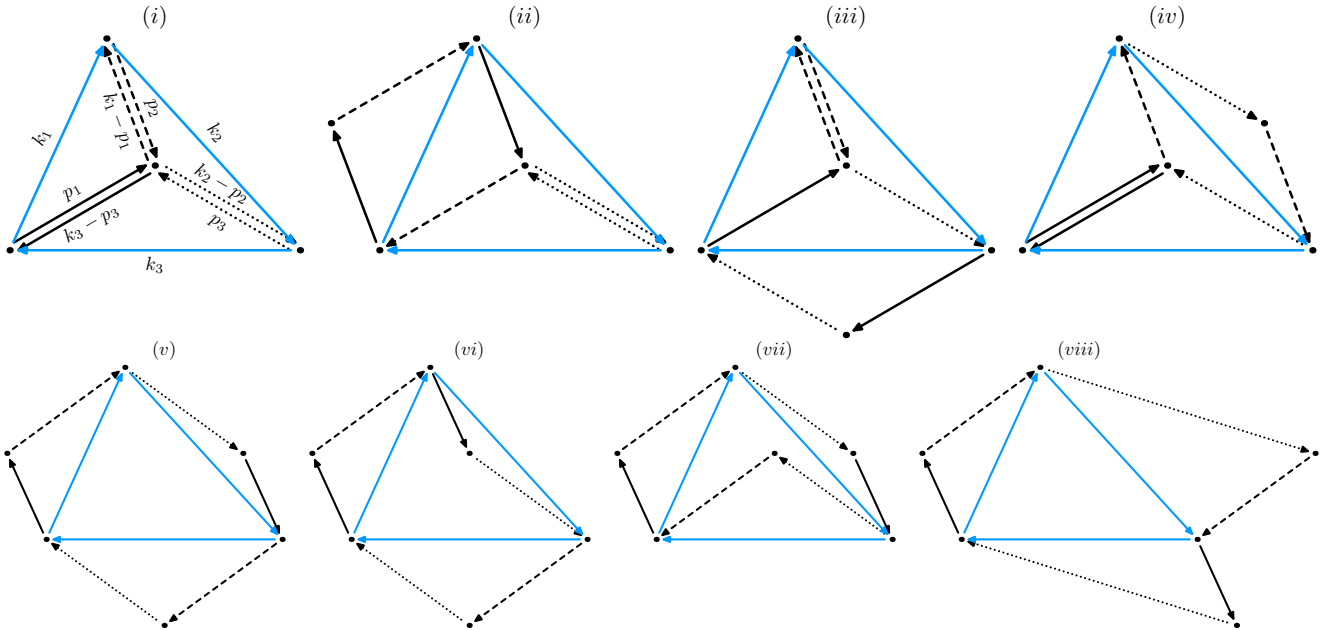


**FIG. 12:** Geometrical configurations for the eight non-vanishing contractions of the three-point function listed in Eq. (B.4).

and  $\delta\dot{h}(t_e) = \delta\dot{h}(t_{\text{RH}})$ , where  $t_e$  is the time at the end of inflation and  $t_{\text{RH}}$  is the time at the beginning of reheating. Assuming a fast reheating essentially amounts to saying that  $t_e \simeq t_{\text{RH}}$ . Across this time boundary, energy is also conserved. At the end of inflation the energy density is

$$\rho_e = \rho_{\text{inf}} + \rho_{h,e} , \quad (\text{C.1})$$

with  $\rho_{\text{inf}} = 3H^2 m_P^2$  and  $\rho_{h,e} = \dot{h}_{c,e}^2/2 + V_0(h_{c,e})$ , with  $h_{c,e} \equiv h_c(t_e)$ . During the instantaneous reheating,  $\rho_{\text{inf}}$  is used up in reheating the plasma (populated through the inflaton decays). The total energy density at  $t_{\text{RH}}$  is

$$\rho_{\text{RH}} = \rho_{\text{pl}} + \rho_{h,\text{RH}} . \quad (\text{C.2})$$

In the plasma rest-frame

$$\rho_{\text{pl}} = \omega - P, \quad (\text{C.3})$$

where  $P$  is the plasma pressure (equal to minus the free-energy density) and

$$\omega = T \frac{\partial P}{\partial T} \quad (\text{C.4})$$

is the enthalpy density. We also have  $\rho_{h,\text{RH}} = \dot{h}_{c,\text{RH}}^2/2 + V_0(h_{c,\text{RH}})$ , with  $h_{c,\text{RH}} \equiv h_c(t_{\text{RH}})$ . It is more convenient to arrange the splitting between plasma and Higgs background energies in a different way, by first separating a pure radiation part in  $\rho_{\text{pl}}$  by writing

$$P = P_\gamma - V_T(h_c, T) \quad (\text{C.5})$$

and

$$\omega = \omega_\gamma - T \frac{\partial V_T}{\partial T}, \quad (\text{C.6})$$

where  $P_\gamma = \pi^2 g_* T^4/90$ ,  $\omega_\gamma = 2\pi^2 g_* T^4/45$  and  $V_T(h_c, T)$  is the field-dependent thermal contribution of the plasma to the Higgs potential. Then, we assign this potential term to the Higgs energy density and write

$$\rho_{\text{pl}} = \frac{\pi^2}{30} g_* T^4 - T \frac{\partial V_T}{\partial T}, \quad \rho_{h,\text{RH}} = \frac{1}{2} \dot{h}_{c,\text{RH}}^2 + V_0(h_{c,\text{RH}}) + V_T(h_{c,\text{RH}}, T). \quad (\text{C.7})$$

The reheating temperature can be obtained from  $\rho_e = \rho_{\text{RH}}$ , which gives  $T_{\text{RH}} \simeq [90/(\pi^2 g_*)]^{1/4} \sqrt{H m_P}$ . The small fluctuations in the Higgs background cause small fluctuations in  $T_{\text{RH}}$ . Using  $V_T \simeq m_T^2 h_c^2/2 = \kappa T^2 h_c^2/2$  we get  $\delta T \simeq 15\kappa h_c \delta h_c / (2\pi^2 g_* T) \ll \delta h$ . By matching the fluctuations in the energy density across  $t_e \simeq t_{\text{RH}}$ , that is,  $\delta\rho_e = \delta\rho_{\text{RH}}$ , we obtain

$$\delta\rho_{h,e} = \delta\rho_{\text{pl}} + \delta\rho_{h,\text{RH}} , \quad (\text{C.8})$$

or, more explicitly,

$$\begin{aligned} \delta \left[ \frac{1}{2} \dot{h}_{c,e}^2 + V_0(h_{c,e}) \right]_h &= \left[ \frac{2\pi^2}{15} g_* T^3 \delta T - 2\kappa T^2 h_{c,\text{RH}} \delta h_{\text{RH}} \right]_{\text{pl}} + \delta \left[ \frac{1}{2} \dot{h}_{c,\text{RH}}^2 + V_0(h_{c,\text{RH}}) + \frac{1}{2} \kappa T^2 h_{c,\text{RH}}^2 \right]_h \\ &= \delta \left[ \frac{1}{2} \dot{h}_{c,\text{RH}}^2 + V_0(h_{c,\text{RH}}) \right]_h , \end{aligned} \quad (\text{C.9})$$

where in the last equality we have used the result for  $\delta T$  above, which leads to a cancellation of the  $\kappa T^2 h_c \delta h$  terms.

Leaving aside Hubble friction, the energy density of plasma and Higgs background field are not conserved separately. We can still split the energy conservation equation  $\dot{\rho}_{\text{tot}} = 0$  in a plasma and a Higgs one, taking into account Higgs decays into the plasma and write

$$\dot{\rho}_h = (\partial\rho_h/\partial h_c) \dot{h}_c = (\square h_c + V') \dot{h}_c = -\gamma_h \dot{h}_c^2 , \quad (\text{C.10})$$

with  $V = V_0 + V_T$ , and  $\gamma_h \simeq 10^{-3} T$  the Higgs decay width, while  $\dot{\rho}_{\text{pl}} = +\gamma_h \dot{h}_c^2$ . The right-hand side in Eq. (C.10) introduces a friction term in the equation of motion for the Higgs field that is initially subleading in comparison with the Hubble friction term that it should also include, but is important for the late time behaviour of the Higgs condensate.

Having understood how to properly deal with the perturbations of the Higgs coupled to the plasma at a given temperature  $T$ , we are now ready to deal with their behaviour in the radiation phase. Introducing Hubble friction and neglecting the decay term we write the equations of motion of the classical value of the Higgs and its linear perturbation still in the flat gauge as

$$\begin{aligned} \ddot{h}_c + \frac{3}{2t} \dot{h}_c + m_T^2 h_c &= 0, \\ \delta \ddot{h}_1 + \frac{3}{2t} \delta \dot{h}_1 + m_T^2 \delta h_1 &= 0. \end{aligned} \quad (\text{C.11})$$

Notice that in the radiation phase the temperature scales as

$$T = T_{\text{RH}} \left( \frac{a_{\text{RH}}}{a} \right) \quad (\text{C.12})$$

and the scale factor follows the rule  $a = a_{\text{RH}} (t/t_{\text{RH}})^{1/2}$ , so that  $H = 1/(2t)$ . One finds

$$h_c(t) = h(t_{\text{RH}}) \sqrt{\frac{t_{\text{RH}}}{t}} \cos [2m_{T_{\text{RH}}} (\sqrt{tt_{\text{RH}}} - t_{\text{RH}})] + \frac{2\dot{h}(t_{\text{RH}}) t_{\text{RH}} + h(t_{\text{RH}})}{2m_{T_{\text{RH}}} \sqrt{tt_{\text{RH}}}} \sin [2m_{T_{\text{RH}}} (\sqrt{tt_{\text{RH}}} - t_{\text{RH}})] , \quad (\text{C.13})$$

and  $\delta h_1$  tracks  $h_c$ . Up to fast oscillations the classical Higgs field scales like

$$h_c(a) \sim \frac{1}{a} \sim T \quad (\text{C.14})$$

and one can show easily that averaging over the fast oscillations one gets  $\langle \dot{h}_c^2 \rangle = \langle m_T^2 h_c^2 \rangle$ , so that

$$\dot{\rho}_h = \dot{h}_c \ddot{h}_c + m_T^2 h_c \dot{h}_c + \frac{1}{2} \dot{m}_T^2 h_c^2 = -3H \dot{h}_c^2 - H m_T^2 h_c^2 , \quad (\text{C.15})$$

and upon averaging one gets

$$\dot{\rho}_h = -4H \rho_h . \quad (\text{C.16})$$

The Higgs before decaying behaves therefore like a relativistic fluid. One obtains also (still in the flat gauge)

$$\rho_h = \rho_h + \delta\rho_{h,1} = m_T^2 h_c^2 + 2m_T^2 h_c \delta h_1 , \quad (\text{C.17})$$

so that

$$\frac{\delta\rho_{h,1}}{\rho_h} = 2\frac{\delta h_1(t)}{h_c(t)} = 2\frac{\delta h_1(t_{\text{RH}})}{h_c(t_{\text{RH}})} = 2\frac{\delta h_1(t_e)}{h_c(t_e)}, \quad (\text{C.18})$$

where in the next-to-last passage we have used the fact that  $\delta h_1$  is tracking  $h_c$  and in the last passage the continuity in the Higgs sector. We have therefore that upon Higgs decay and using  $\delta\dot{\rho}_{h,1} = -4H\delta\rho_{h,1}$ ,

$$\begin{aligned} -\zeta_1(t_{\text{dec}}) &= H\frac{\delta\rho_1(t_{\text{dec}})}{\dot{\rho}(t_{\text{dec}})} = Hr_h(t_{\text{dec}})\frac{\delta\rho_{h,1}(t_{\text{dec}})}{\dot{\rho}_h(t_{\text{dec}})} = -\frac{r_h(t_{\text{dec}})}{4}\frac{\delta\rho_{h,1}(t_{\text{dec}})}{\rho_h(t_{\text{dec}})} \\ &= -\frac{r_h(t_{\text{dec}})}{2}\frac{\delta h_1(t_{\text{RH}})}{h_c(t_{\text{RH}})} = -\frac{r_h(t_{\text{dec}})}{2}\frac{\delta h_1(t_e)}{h_c(t_e)} = -\frac{r_h(t_{\text{dec}})}{2}\frac{\dot{h}_c(t_e)}{Hh_c(t_e)}\zeta_{h,1}(t_e), \end{aligned} \quad (\text{C.19})$$

where we have made use of the fact that during inflation

$$-\zeta_{h,1} = H\frac{\delta\rho_{h,1}}{\dot{\rho}_h} = H\frac{\delta h_1}{\dot{h}_c}. \quad (\text{C.20})$$

In particular, notice that  $\zeta_h$  during inflation does not coincide with the value during reheating,  $\zeta_h \simeq (\delta h_1/2h_c)$ , signalling that  $\zeta_h$  is not conserved during the transition. This is not surprising, as the Higgs interacts with the hot plasma to suddenly acquire a plasma mass and therefore is not an isolated fluid. The final power spectrum reads

$$\mathcal{P}_\zeta(t_{\text{dec}}) = \frac{k^3}{2\pi^2}|\zeta_k(t_{\text{dec}})|^2 = \frac{r_h^2(t_{\text{dec}})}{4}\left(\frac{H}{2\pi}\right)^2\left(\frac{\dot{h}_c(t_e)}{h_c(t_e)\dot{h}_c(t_k)}\right)^2. \quad (\text{C.21})$$

#### Appendix D: Analytical results for the functions $\mathcal{I}_c, \mathcal{I}_s$

To write down the analytical formulæ for the integrals  $\mathcal{I}_c, \mathcal{I}_s$  defined in Eq. (33) we use the indefinite integrals  $i_c(d, s, \tau)$  and  $i_s(d, s, \tau)$ , so that  $\mathcal{I}_c(d, s) = i_c(d, s, \tau)|_1^\infty$  and a similar formula for  $\mathcal{I}_s$ . We get

$$\begin{aligned} i_c(d, s, \tau) &= \frac{288}{(s^2 - d^2)^3} \left\{ [A(s) \cos \tau + C(d, s) \sin \tau] \cos(d\tau) - [A(d) \cos \tau + C(s, d) \sin \tau] \cos(s\tau) \right. \\ &\quad + [(2/\tau^2) \cos \tau + B(s) \sin \tau] d \sin(d\tau) - [(2/\tau^2) \cos \tau + B(d) \sin \tau] s \sin(s\tau) \\ &\quad \left. + \frac{1}{8}(s^2 + d^2 - 2)^2 (\text{Si}[(1-s)\tau] + \text{Si}[(1+s)\tau] - \text{Si}[(1+d)\tau] - \text{Si}[(1-d)\tau]) \right\}, \end{aligned} \quad (\text{D.1})$$

and

$$\begin{aligned} i_s(d, s, \tau) &= \frac{288}{(s^2 - d^2)^3} \left\{ [A(s) \sin \tau - C(d, s) \cos \tau] \cos(d\tau) + [-A(d) \sin \tau + C(s, d) \cos \tau] \cos(s\tau) \right. \\ &\quad + [(2/\tau^2) \sin \tau - B(s) \cos \tau] d \sin(d\tau) + [-(2/\tau^2) \sin \tau + B(d) \cos \tau] s \sin(s\tau) \\ &\quad \left. + \frac{1}{8}(s^2 + d^2 - 2)^2 (\text{Ci}[(1+d)\tau] + \text{Ci}[(1-d)\tau] - \text{Ci}[|s-1|\tau] - \text{Ci}[(1+s)\tau]) \right\}, \end{aligned} \quad (\text{D.2})$$

where  $\text{Si}(x)$  is the sine integral function,  $\text{Ci}(x)$  is the cosine integral function and

$$A(x) \equiv \frac{1}{\tau^3} [2 + (x^2 - 1)\tau^2], \quad B(x) \equiv \frac{1}{\tau^3} [6 + (x^2 - 1)\tau^2], \quad C(x, y) \equiv \frac{1}{\tau^4} [6 - (1 + 2x^2 - y^2)\tau^2]. \quad (\text{D.3})$$

Noting that

$$i_c(d, s, \infty) = -36\pi \frac{(s^2 + d^2 - 2)^2}{(s^2 - d^2)^3} \theta(s-1), \quad i_s(d, s, \infty) = 0, \quad (\text{D.4})$$

we get

$$\mathcal{I}_c(d, s) = \frac{288}{(s^2 - d^2)^3} \left\{ [2c_1 + (5 + d^2)s_1] s \sin s - [2c_1 + (5 + s^2)s_1] d \sin d \right.$$

$$+ [(1 + d^2)c_1 + (5 + d^2 - 2s^2)s_1] \cos s - [(1 + s^2)c_1 + (5 + s^2 - 2d^2)s_1] \cos d + \frac{1}{8}(s^2 + d^2 - 2)^2 [\text{Si}(1 + d) + \text{Si}(1 - d) - \text{Si}(1 - s) - \text{Si}(1 + s) - \pi\theta(s - 1)] \Big\}, \quad (\text{D.5})$$

where  $c_1 \equiv \cos(1) \simeq 0.54$ ,  $s_1 \equiv \sin(1) \simeq 0.84$  and

$$\mathcal{I}_s(d, s) = \frac{288}{(s^2 - d^2)^3} \Big\{ [2s_1 - (5 + d^2)c_1] s \sin s + [-2s_1 + (5 + s^2)c_1] d \sin d + [(1 + d^2)s_1 - (5 + d^2 - 2s^2)c_1] \cos s + [-(1 + s^2)s_1 + (5 + s^2 - 2d^2)c_1] \cos d - \frac{1}{8}(s^2 + d^2 - 2)^2 [\text{Ci}(1 + d) + \text{Ci}(1 - d) - \text{Ci}(|1 - s|) - \text{Ci}(1 + s)] \Big\}. \quad (\text{D.6})$$

If instead of the lower integration limit  $\tau_0 = 1$  one takes  $\tau_0 = 0$ , using

$$i_c(d, s, 0) = 0, \quad i_s(d, s, 0) = 36 \frac{(s^2 + d^2 - 2)}{(s^2 - d^2)^2} \left[ \frac{(s^2 + d^2 - 2)}{(s^2 - d^2)} \log \frac{(1 - d^2)}{|s^2 - 1|} + 2 \right], \quad (\text{D.7})$$

one gets

$$\hat{\mathcal{I}}_c(d, s) \equiv i_c(d, s, \tau)|_0^\infty = -36\pi \frac{(s^2 + d^2 - 2)^2}{(s^2 - d^2)^3} \theta(s - 1), \quad (\text{D.8})$$

$$\hat{\mathcal{I}}_s(d, s) \equiv i_s(d, s, \tau)|_0^\infty = -36 \frac{(s^2 + d^2 - 2)}{(s^2 - d^2)^2} \left[ \frac{(s^2 + d^2 - 2)}{(s^2 - d^2)} \log \frac{(1 - d^2)}{|s^2 - 1|} + 2 \right].$$

All our results for the sourced gravitational waves and their power spectrum are in agreement with Ref. [36]. The only difference is in the lower limit of integration, which they have taken to be  $\tau_0 = 0$  as in Eq. (D.8). In our numerical results in this paper, we have instead chosen  $\tau_0 = 1$  as in Eqs. (D.5) and (D.6). Strictly speaking,  $\tau_0 = 0$  is the correct choice, but given that the source is damped on super-Hubble scales, the time integral receives the main contribution for  $\tau \gtrsim 1$ , and the final numerical difference is not particularly important.

We have also compared our results with [21], finding some differences. In particular, their formulæ for the power spectrum of GWs differ from ours by a total prefactor of  $\frac{16}{81} \frac{32k^2}{\pi^4} = 0.06k^2$  that they introduced throughout their derivation, the sum over  $k$  in their Eq. (26) should start from  $k = 0$  and a few of the entries of the matrices  $M_{mn}^i$  contain some typos.

- 
- [1] B. P. Abbott et al. [LIGO Scientific and Virgo Collaborations], Phys. Rev. Lett. **116** (2016) 061102 [[gr-qc/1602.03837](#)].
- [2] M. Sasaki, T. Suyama, T. Tanaka and S. Yokoyama, [[astro-ph.CO/1801.05235](#)].
- [3] C. Caprini and D. G. Figueroa, [[astro-ph.CO/1801.04268](#)].
- [4] N. Bartolo *et al.*, JCAP **1612** (2016) no. 12, 026 [[astro-ph.CO/1610.06481](#)].
- [5] B. Sathyaprakash *et al.*, Class. Quant. Grav. **29**, 124013 (2012) Erratum: [Class. Quant. Grav. **30**, 079501 (2013)] [[gr-qc/1206.0331](#)].
- [6] D. Hoakon [Ligo Scientific Collaboration], Nuovo Cim. C **40**, no. 3, 119 (2017).
- [7] B. P. Abbott *et al.* [LIGO Scientific Collaboration], Class. Quant. Grav. **34**, no. 4, 044001 (2017) [[astro-ph.IM/1607.08697](#)].
- [8] M. Sher, Phys. Rept. **179** (1989) 273; P.B. Arnold, Phys. Rev. D **40** (1989) 613; G. Altarelli and G. Isidori, Phys. Lett. B **337** (1994) 141; J.A. Casas, J.R. Espinosa and M. Quirós, Phys. Lett. B **382** (1996) 374 [[hep-ph/9603227](#)]; T. Hambye and K. Riessellmann, Phys. Rev. D **55** (1997) 7255 [[hep-ph/9610272](#)]; G. Isidori, G. Ridolfi and A. Strumia, Nucl. Phys. B **609** (2001) 387 [[hep-ph/0104016](#)]; J. Ellis, J.R. Espinosa, G.F. Giudice, A. Hoecker and A. Riotto, Phys. Lett. B **679** (2009) 369 [[hep-ph/0906.0954](#)]; F. Bezrukov, M. Y. Kalmykov, B. A. Kniehl and M. Shaposhnikov, JHEP **1210** (2012) 140 [[hep-ph/1205.2893](#)]; A.V. Bednyakov, B.A. Kniehl, A.F. Pikelner and O.L. Veretin, Phys. Rev. Lett. **115** (2015) 201802 [[hep-ph/1507.08833](#)].
- [9] J. Elias-Miró, J.R. Espinosa, G.F. Giudice, G. Isidori, A. Riotto and A. Strumia, Phys. Lett. B **709** (2012) 222 [[hep-ph/1112.3022](#)]; G. Degrassi, S. Di Vita, J. Elias-Miró, J.R. Espinosa, G.F. Giudice, G. Isidori and A. Strumia, JHEP **1208** (2012) 098 [[hep-ph/1205.6497](#)]; D. Buttazzo, G. Degrassi, P.P. Giardino, G.F. Giudice, F. Sala, A. Salvio and A. Strumia, JHEP **1312** (2013) 089 [[hep-ph/1307.3536](#)].
- [10] A. Salvio, A. Strumia, N. Tetradis and A. Urbano, JHEP **1609** (2016) 054 [[hep-ph/1608.02555](#)].
- [11] J. R. Espinosa, D. Racco and A. Riotto, Phys. Rev. Lett. **120**, 121301 (2018) [[hep-ph/1710.11196](#)].
- [12] D.H. Lyth and A. Riotto, Phys. Rept. **314** (1999) 1 [[hep-ph/9807278](#)].



- [13] J.R. Espinosa, G.F. Giudice and A. Riotto, JCAP **0805** (2008) 002 [[hep-ph/0710.2484](#)].
- [14] A. Kobakhidze and A. Spencer-Smith, Phys. Lett. B **722** (2013) 130 [[hep-ph/1301.2846](#)]; [[hep-ph/1404.4709](#)]; M. Fairbairn and R. Hogan, Phys. Rev. Lett. **112** (2014) 201801 [[hep-ph/1403.6786](#)]; K. Enqvist, T. Meriniemi and S. Nurmi, JCAP **1407** (2014) 025 [[hep-ph/1404.3699](#)]; A. Hook, J. Kearney, B. Shakya and K.M. Zurek, JHEP **1501** (2015) 061 [[hep-ph/1404.5953](#)]; K. Kamada, Phys. Lett. B **742** (2015) 126 [[hep-ph/1409.5078](#)]; A. Shkerin and S. Sibiryakov, Phys. Lett. B **746** (2015) 257 [[hep-ph/1503.02586](#)]; J. Kearney, H. Yoo and K.M. Zurek, Phys. Rev. D **91** (2015) 12, 123537 [[hep-th/1503.05193](#)]; W.E. East, J. Kearney, B. Shakya, H. Yoo and K.M. Zurek, Phys. Rev. D **95** (2017) 023526 [[hep-ph/1607.00381](#)].
- [15] M. Herranen, T. Markkanen, S. Nurmi and A. Rajantie, Phys. Rev. Lett. **113** (2014) 211102 [[hep-ph/1407.3141](#)].
- [16] J.R. Espinosa, G.F. Giudice, E. Morgante, A. Riotto, L. Senatore, A. Strumia and N. Tetradis, JHEP **1509** (2015) 174 [[hep-ph/1505.04825](#)].
- [17] Y. Ema, K. Mukaida and K. Nakayama, JCAP **1610** (2016) 043 [[hep-ph/1602.00483](#)]; K. Kohri and H. Matsui, Phys. Rev. D **94** (2016) 103509 [[hep-ph/1602.02100](#)]; K. Enqvist, M. Karciauskas, O. Lebedev, S. Rusak and M. Zatta, JCAP **1611** (2016) 025 [[hep-ph/1608.08848](#)]; M. Postma and J. van de Vis, JCAP **1705** (2017) 004 [[hep-ph/1702.07636](#)]; Y. Ema, M. Karciauskas, O. Lebedev and M. Zatta, JCAP **1706** (2017) 054 [[hep-ph/1703.04681](#)]; A. Joti, A. Katsis, D. Loupas, A. Salvio, A. Strumia, N. Tetradis and A. Urbano, JHEP **1707** (2017) 058 [[hep-ph/1706.00792](#)]; A. Rajantie and S. Stopyra, Phys. Rev. D **97** (2018) no. 2, 025012 [[hep-th/1707.09175](#)]; D.G. Figueroa, A. Rajantie and F. Torrenti, [[astro-ph.CO/1709.00398](#)].
- [18] N. Bartolo, V. De Luca, G. Franciolini, A. Lewis, M. Peloso and A. Riotto, [[astro-ph.CO/1810.12218](#)]; N. Bartolo, V. De Luca, G. Franciolini, M. Peloso, D. Racco and A. Riotto, [[astro-ph.CO/1810.12224](#)].
- [19] V. Acquaviva, N. Bartolo, S. Matarrese and A. Riotto, Nucl. Phys. B **667** (2003) 119 [[astro-ph/0209156](#)].
- [20] S. Mollerach, D. Harari and S. Matarrese, Phys. Rev. D **69** (2004) 063002 [[astro-ph/0310711](#)].
- [21] K. N. Ananda, C. Clarkson and D. Wands, Phys. Rev. D **75** (2007) 123518 [[gr-qc/0612013](#)].
- [22] D. Baumann, P. J. Steinhardt, K. Takahashi and K. Ichiki, Phys. Rev. D **76** (2007) 084019 [[hep-th/0703290](#)].
- [23] R. Saito and J. Yokoyama, Prog. Theor. Phys. **123** (2010) 867 Erratum: [Prog. Theor. Phys. **126** (2011) 351] [[astro-ph.CO/0912.5317](#)].
- [24] K. Ando, K. Inomata, M. Kawasaki, K. Mukaida and T. T. Yanagida, [[astro-ph.CO/1711.08956](#)].
- [25] M. Maggiore, Phys. Rept. **331** (2000) 283 [[gr-qc/9909001](#)].
- [26] N. Bartolo *et al.*, JCAP **1612**, no. 12 (2016) 026 [[astro-ph.CO/1610.06481](#)].
- [27] G. Aad *et al.* [ATLAS and CMS Collaborations], Phys. Rev. Lett. **114** (2015) 191803 [[hep-ex/1503.07589](#)].
- [28] V. Khachatryan *et al.* [CMS Collaboration], Phys. Rev. D **93** (2016) no.7, 072004 [[hep-ex/1509.04044](#)]; The ATLAS collaboration [ATLAS Collaboration], ATLAS-CONF-2017-071.
- [29] H. Audley *et al.*, [[astro-ph.IM/1702.00786](#)].
- [30] C. Caprini *et al.*, JCAP **1604** (2016) no.04, 001 [[astro-ph.CO/1512.06239](#)].
- [31] B. P. Abbott *et al.* [LIGO Scientific and Virgo Collaborations], Phys. Rev. Lett. **118** (2017) no.12, 121101 Erratum: [Phys. Rev. Lett. **119** (2017) no.2, 029901] [[gr-qc/1612.02029](#)].
- [32] C. J. Moore, R. H. Cole and C. P. L. Berry, Class. Quant. Grav. **32** (2015) no.1, 015014 [[gr-qc/1408.0740](#)]; B. S. Sathyaprakash and B. F. Schutz, Living Rev. Rel. **12** (2009) 2 [[gr-qc/0903.0338](#)]; Einstein Telescope, design at <http://www.et-gw.eu/>.
- [33] S. Dimopoulos, P. W. Graham, J. M. Hogan, M. A. Kasevich and S. Rajendran, Phys. Lett. B **678** (2009) 37 [[gr-qc/0712.1250](#)]; P. W. Graham, J. M. Hogan, M. A. Kasevich and S. Rajendran, Phys. Rev. Lett. **110** (2013) 171102 [[quant-ph/1206.0818](#)]; J. Coleman [MAGIS-100 Collaboration], [[physics.ins-det/1812.00482](#)]; O. Buchmuller, “The atom interferometer observatory network”, 2018.
- [34] E. Thrane, Phys. Rev. D **87** (2013) no.4, 043009 [[astro-ph.IM/1301.0263](#)].
- [35] J. R. Espinosa, D. Racco and A. Riotto, Eur. Phys. J. C **78** (2018) no.10, 806 [[hep-ph/1804.07731](#)].
- [36] K. Kohri and T. Terada, Phys. Rev. D **97** (2018) no.12, 123532 [[gr-qc/1804.08577](#)].